**NTNU – Trondheim**
Norwegian University of
Science and Technology

# Micro-Photoluminescence Spectroscopy of Au-assisted MBE Grown AlGaAs Nanowires with Axial GaAs Inserts

**Markus Solberg Wahl**

Nanotechnology
Submission date: June 2012
Supervisor: Helge Weman, IET

Norwegian University of Science and Technology
Department of Electronics and Telecommunications

# ABSTRACT

Wurtzite (WZ) GaAs is at present not well studied. There is controversy among properties such as bandgap, band symmetry and exciton binding energy. Two approaches to solve the problem exist: To grow WZ GaAs nanowires (NWs) and measure them directly, or to grow WZ GaAs inserts into a larger bandgap material. The latter approach was used in this study, where the system was investigated with polarization, temperature and time-resolved photoluminescence (PL) spectroscopy. The NWs were prepared on a sample allowing for further study with transmission electron microscopy (TEM). Based on energy, temperature dependence of the emission energy and polarization, the free exciton in WZ GaAs was found to be discernible at low temperatures. The GaAs inserts were also found to exhibit quantum confinement effects, that could be caused by the reservoir effect in molecular-beam epitaxy (MBE) growth.

# SAMMENDRAG

Wurtzite (WZ) GaAs er hittil ikke et godt undersøkt material. Det er fortsatt stor uenighet om dets egenskaper f.eks. båndgap, båndsymmetri og bindingsenergi for eksitoner. Det finnes to fremgangsmåter for å undersøke disse egenskapene nærmere: Å gro WZ GaAs nanotråder og måle dem direkte, eller å gro WZ GaAs segmenter inne i materialer med høyere båndgap. Denne studien bruker sistnevnte metode. Systemet ble undersøkt med polarisasjons-, temperatur- of tidsoppløst fotoluminescens spektroskopi. Ved å se på energien, og emisjonsenergiens temperatur- og polarisasjonsavhengighet, ble frie eksitoner i WZ GaAs identifisert ved lave temperaturer. Det ble også påvist kvantebegrensnings-effekter i GaAs-segmentene. Dette kan være forårsaket av reservoir-effekten, som kan oppstå under groing i molekyl-stråle epitaksi (MBE).

CONTENTS

# ACKNOWLEDGEMENTS

In the process of writing my master thesis there are many people to whom I am grateful. First of all I want to thank my supervisor, Prof. Helge Weman for giving me the opportunity to work in his laboratory and for including me in his research group. His advice on the interpretation of my results were invaluable.

I would also like to thank my co-supervisor Lyubomir Ahtapodov, for always having a thought through answer to my questions and precise explanations to the physical phenomena encountered. Without the time and effort he has put in, and his ready mind, this work would not have been possible.

My friends and family have all been important to me in this process, and I would like to thank them all. My physical deterioration this semester has been slowed down by Thomas and Johannes, for which I want to thank them. The time with them was combined with good company, of course, but also precious advice. During stressful and exhausting times, my good friends Øyvind and Torstein have supplied me with a perfect work environment in their home. I want to thank them both for letting me live with them and for all the nice moments we have shared this semester. I also want to thank Julie, who has made sure I had a social life in this time, and been there for me and motivated me all the way. Andreas, my brother, has dropped in occasionally and helped reducing the physical distance to my family. The short moments we shared, helped me to get a better perspective on both my thesis and life in general.

Finally, I want to thank my personal spell-checker, personal motivator, expert problem fixer and good friend, which I would normally call my mother. She is the most important person in my life.

*Markus Solberg Wahl*
*Trondheim, June 2012*

# 1. INTRODUCTION

In the last 10 years research on semiconductor nanowires (NW) has grown exponentially [1]. Expectations for the future development of this field are immense. NWs are a natural choice in the quest for downscaling SC devices, and have already been used in transistors [2], sensors, lasers [3], light-emitting diodes [4] and solar panels [5]. One of the practical advantages with quasi-1D structures is their ability to accommodate lattice strain significantly more efficient than quantum well structures [6][7]. This allows for a wide selection of heterostructures previously out of reach, for example the integration of III-V materials on Si has long been inhibited by this problem. In addition to new design possibilities [7], the interest in NW based devices comes from an increased quantum efficiency, caused by a reduced defect density and quantum confinement.

Although a large amount of research is aimed at exploiting the possibilities NWs have to offer, there are many fundamental properties yet to be explored. For instance, the bandgap width and the conduction band symmetry in wurtzite (WZ) GaAs are still debated [8][9][10]. The goal of this study is to further investigate these uncertainties, through the use of GaAs inserts in AlGaAs NWs. These were invented to overcome the problem of axial AlGaAs in the GaAs-AlGaAs core-shell NWs, normally worked with, and to achieve stacking free WZ GaAs. The Au-assisted molecular-beam epitaxy (MBE) grown NWs are intended to contain nominally bulk GaAs inserts, which are expected to be nearly free of defects.

# 2. THEORY

The theory described in this section is meant to create a basis for the interpretations and discussions in Sec. 5. First, an introduction to band theory is presented in combination with the band structure in GaAs. The investigated AlGaAs NWs with axial GaAs inserts are then treated in light of the first section. Selected parts from the field of solid-state physics, which are considered important, are then presented. Connections to the phenomena observed in the measurements are mentioned. Finally, the physical aspects of the measurement technique photoluminescence spectroscopy) are considered.

## *2.1 Band structure*

Semiconductor materials are generally described through their electronic band structure e.g. the dispersion relation. Materials in this category have a highest-occupied energy band, the valence band (VB), and a lowest-unoccupied energy band, the conduction band (CB), separated by a region of forbidden states called the bandgap [11][12]. The bandgap energy ($E_g$) is defined as the difference between the top and bottom of the VB and CB, respectively [13].

A crystal is characterized by its constituents and its symmetry. To describe a crystals symmetry, the operations which leave the unit cell invariant are considered. The group of symmetry operations which are possible for a crystal is called its *point group*, where each symmetry operation can be represented by an operator.

Crystals symmetries become important when noting that symmetry operations commute with the Hamiltonian [14]. This can be expressed as $P(X_i)H = HP(X_i)$, where $X_i \in G$ is an element of the point-group $G$ and $P(X_i)$ is an operator corresponding to $X_i$. This means that $P(X_i)$ and $H$ will have a common set of wavefunctions i.e. if $H\Psi_{\alpha j} = E_\alpha$, then $P(X_i)\Psi_{\alpha j}$ will also be an eigenfunction with eigenvalue $E_\alpha$. However, because of the hermiticity of the Hamiltonian, the set $\{\Psi_{\alpha j}\}$ is a complete

set. Hence, $P(X_i)\Psi_{\alpha j}$ must be a linear combination of the other $\{\Psi_{\alpha j}\}$. Mathematically this can be expressed

$$P(X_i)\Psi_{\alpha k} = \sum \Gamma_\alpha(X_i)_{jk}\Psi_{\alpha j}. \tag{2.1}$$

Since this holds for all $X_i$ it is evident that $\Gamma_\alpha(X_i)$ is a matrix representation of the point-group of $H$. This gives the correspondence between crystal symmetries and band structure; $E_\alpha$ is said to have the symmetry $\Gamma_\alpha$.

This relation becomes important when selection rules (Sec. 2.4.2) for a transition are considered. The incident field, the initial and final state i.e. their $\Gamma$'s can now be used to calculate whether a transition is allowed or not.

The bandstructure of bulk WZ GaAs (Fig. 2.1) has been calculated empirically, using pseudopotentials [6]. The calculation is based on experimental values at high symmetry points in ZB GaAs, which are used to calibrate the model. With the appropriate crystal structure factors, these pseudopotentials are transferred to the WZ pseudopotential Hamiltonian, which is used in the bandstructure calculation. The predicted bandgap of 1.503 eV is a little lower than what is found in experimental studies [10][8].

[6] predicts that the lowest conduction band has $\Gamma_8$-symmetry, while [10] shows with Resonnant Raman spectroscopy it has $\Gamma_7$-symmetry. This discrepancy is stated by the authors of [10]. Recent studies at NTNU places the $\Gamma_8$ band as the lowest by showing that it does not behave like a $\Gamma_7$-band [15].

One of the main differences between the WZ and ZB structures is the doubled unit cell length along the [111] direction [16]. In the WZ unit cell there are four atoms in this direction, whereas the ZB structure has two. It is therefore expected that the WZ band structure can be approximated by folding the ZB structure along the $\Lambda$ direction, from the midpoint between the zone center and the L zone edge [17]. From this, a multiplication of the optically active transitions is expected [18]. New zone center transitions are thus expected e.g. from the L-point in ZB [17][6].

## *2.2 Material properties of GaAs*

With a direct bandgap and high electron mobility, GaAs has become a widely used material in semiconductor technology with large expectations for future applications [19]. Implementation with other III-V semiconductors is done with little difficulty, as lattice matching is readily achieved

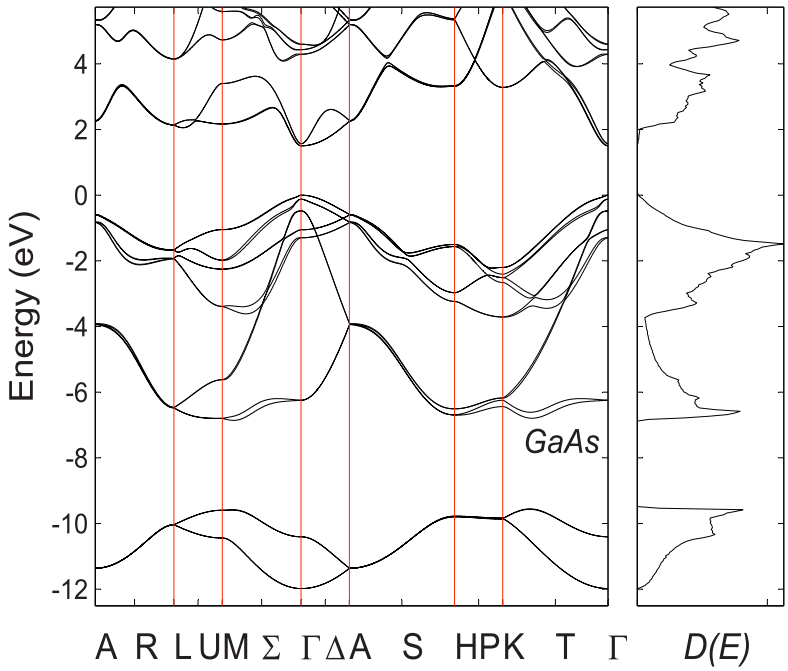


*Fig. 2.1:* Predicted WZ GaAs band structure, calculated with empirical pseudopotentials including spin-orbit coupling [6]. The (direct) bandgap is found at the Γ-point and is calculated to 1.503 eV. High symmetry points are labelled on the axis and the density of states is shown in the right plot.

between materials with the same crystal structure. GaAs is known to exhibit a ZB crystal structure in bulk, while confined systems may result in a WZ structure (Sec. 2.2.2) [6]. The crystal structure can be controlled by varying the nanowire diameter and growth temperature [20]. However, the crystal structure mostly features switching between the two phases and other irregularities.

### *2.2.1 AlGaAs nanowires with GaAs inserts*

The NWs studied, are Au-assisted MBE grown AlGaAs NWs containing an axial segment (d = 80 nm, l = 100 nm) of GaAs. The GaAs inserts are grown by switching the chamber composition to GaAs for 2 min. In growing the rest of the AlGaAs wire, radial growth proceeds as well, creating an AlGaAs shell round the insert. Finally, a thin GaAs layer is grown to passivate the material. The insert should lie 1-1.5 $\mu$m below the Au catalyst particle.

The GaAs inserts are grown with a diameter of around 80 nm, which by far exceeds the exciton Bohr radius (12 nm [21]). The inserts are therefore expected to act as bulk GaAs i.e. not exhibit quantum confinement effects. Dependent on temperature and radius, the NW growth proceeds as ZB or WZ. From a thermodynamic point of view, the surface energy of {1100} WZ planes is smaller than the {110} and {111}A/B planes of ZB [22]. In NWs with small radii the surface energy dominates and a WZ crystal structure is therefore expected. From the growth conditions the crystal structure studied here is expected to be WZ.

The dielectric mismatch effect favours emission and absorption along the NW axis [23]. However, selection rules (Sec. 2.4.2) apply in band-band transitions, hence limiting the allowed photoluminescence (PL) polarization. The selection rules state that WZ crystals emit perpendicularly polarized with respect to the NW, while ZB crystals may emit both parallel and perpendicular to the NW [22][9]. Because of the dielectric effect, however, the emission is predominantly parallel in ZB [9]. In pure WZ, the perpendicular emission is depolarized in comparison to ZB GaAs, because of the same effect.

Reference [9] has claimed that stacking faults and twin planes influence the polarization. The authors found that with a low concentration of stacking faults, the polarization remains perpendicular, while it becomes more parallel for high concentrations. Small segments of ZB also add a parallel component to the polarization. Since the selection rules are different in cubic (ZB) and hexagonal (WZ) lattices, group theory does not apply. The

approach for the calculation of selection rules is therefore unclear and one has to rely on experimental results. Stacking faults in WZ NWs can be seen as a single segment of a ZB crystal phase, while the same in ZB results in a twin plane [20]. Structures with a random mixture of the two phases are called polytypic.

ZB and WZ GaAs exhibit similar bandgaps ($\sim$1.515 eV [8]), but relative to the vacuum level they have different offsets, see Fig. 2.2. At interfaces between the two crystal structures, type II transitions are hence possible (Fig. 2.2b). The emission energy of this transition is lowered by an amount equal to conduction band offset, with respect to a type I transition. The figure also shows that a stacking fault i.e. a single segment of ZB in a WZ crystal, will act as a quantum well (QW) and confine charge carriers (Fig. 2.2d). Because of the quantum confinement in the QW, the energy levels are elevated (Sec. 2.3.3) and photon emission therefore appears at wavelengths somewhere between type I and type II transitions. According to [9], the perpendicular nature of the emissions should remain intact.

When the defect plane concentration is high, the hole in the WZ valence band (VB) may be confined as well (Fig. 2.2e). This again raises the energy, which may result in emission energies similar to the bandgap. The emissions are now not strictly perpendicular, according to [9].

The AlGaAs-GaAs heterojunction forms a type I band structure because of the larger AlGaAs bandgap. Close to the interface the field-effect will draw charge carriers towards the GaAs insert, but charge transport in the rest of the wire is diffusion controlled. The decreasing Al content along the NW axis, in the tip direction, impedes diffusion and causes a graded bandgap. Along with expected disorder effects, this explains why the AlGaAs signal is low.

### *2.2.2 Crystal structure of GaAs*

The ZB crystal is formed by two interpenetrating face-centered-cubic (fcc) Bravais lattices (each of a different atomic species, denoted A and B), whereas the WZ structure is constructed from two interpenetrating hexagonal-close-packed (hcp) lattices [6]. The difference is easily seen by considering the structures along the [111] direction, along which both lattices look like stacked hexagonal layers, as can be seen in Fig. 2.3a,b. Each layer consists of identical atoms, which alternates between anions and cations. The $[111]_{\mathrm{ZB}}/[0001]_{\mathrm{WZ}}$ directions in the two phases, coincides with the NW growth axis, which in WZ is the optic axis. That nine of the 12 nearest neighbours are the same, suggest that the electronic environment in the

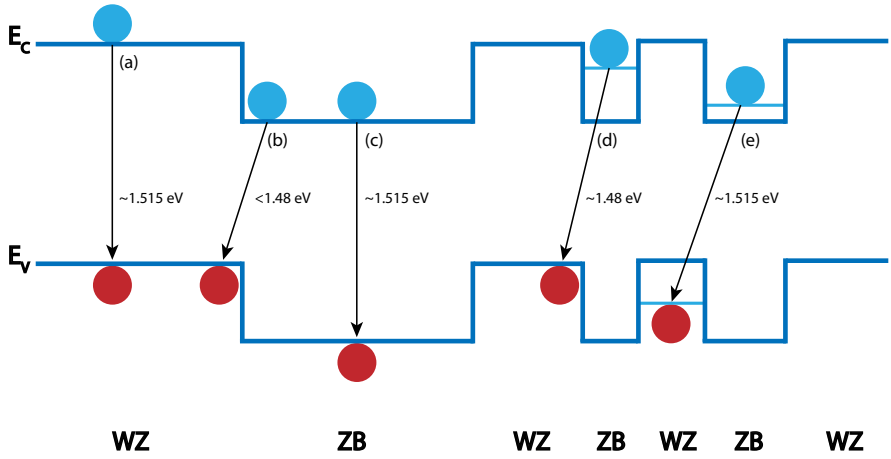


*Fig. 2.2:* Band alignment at the wurtzite (WZ)/zincblende (ZB) heterointerface. Approximate/indicative energies for GaAs are shown. The crystal phases exhibit type II-staggered band alignment with spatially separated electrons and holes. (a) and (c) shows type I transitions in WZ and ZB, respectively. A type II transition (b) happens when an electron in the ZB conduction band recombines with a hole in the WZ valence band. Quantum confinement raises the electron (d) or electron and hole (e) energies, which in case (e) gives emission energies similar to the bandgap.

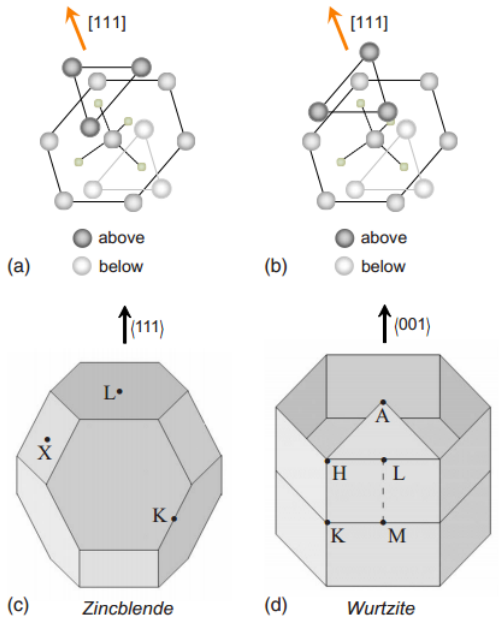


*Fig. 2.3:* Crystal structure of the zincblende (a) and wurtzite (b) crystal structure. The large spheres represent one atom specie. Along the [111] direction both lattices consist of stacked hexagonal layers. Nine of the 12 nearest neighboors are in the same position, the last three are rotated by $\pi/3$. (c) is the Brilluoin zone for zincblende and (d) is the Brilluoin zone for wurtzite. The $\Gamma$ points are at the center of the Brilluoin zones. [6]

two polytypes is similar. The crystal potentials will therefore be almost identical in ZB and WZ.

As can be seen in Fig. 2.3, one can describe ZB and WZ in the [111] and [0001] direction as hexagonal layers in the order ABCABC and ABAB, respectively. The C-layer in ZB corresponds to the A-layer rotated by $\pi/3$. In a WZ crystal, misplacement of a single bilayer gives the structure AB AB|CBCB, where the line represents the defect plane [20]. This is called a stacking fault because of the single ABC unit. However, in the ZB phase, misplacement of a single bilayer creates a twin plane.

## *2.3 Important Concepts from Solid-State Physics*

To understand the physical properties observed in the measurements, a series of fundamental concepts are introduced. Their connections to other

effects are indicated when they appear.

### 2.3.1 Effective mass

Because the charge carriers in a crystal can be seen as waves in a periodic potential, the effective mass differs from that in free space. Close to band extrema, the dispersion is approximately parabolic and can hence be Taylor expanded. Close to extrema, the linear term can be neglected, and the expansion becomes,

$$E(\vec{k}) = E(\vec{k_0}) + \frac{1}{2}\sum \frac{d^2E}{dk_i dk_j}(k_i - k_{0i})(k_j - k_{0j}). \tag{2.2}$$

Since only the relative energy is important, the constant term can be set to zero. The dispersion can therefore be written,

$$E = \frac{1}{m^*}(p - p_0)^2, \tag{2.3}$$

where m* can be expressed through the inverse effective mass tensor:

$$(m^*)^{-1}_{ij} = \hbar^2 \sum \frac{d^2E}{dk_j dk_j}. \tag{2.4}$$

It follows that the effective mass is directly related to the band curvature. Thus, at band minima the effective mass is positive, while at band maxima it is negative. The latter can be interpreted by looking at the expression for current density, $\vec{j} = \frac{en\vec{p}}{m^*}$. It follows (since e$<$ 0) that negative mass can be interpreted as positively charged particles moving in the current direction. The quasi-particle is called a hole is a phenomenon only present at band extrema.

### 2.3.2 Density of states

When the band structure of the material is known, the density of states (DOS) can be found be by integrating over a shell corresponding to an infinitesimal increase in energy, $\{E(\vec{k}), E(\vec{k}) + dE\}$, in $k$-space,

$$dZ = \frac{V}{(2\pi)^3}\int_E^{E+dE} d\vec{k} \tag{2.5}$$

where the factor in front is the density of states in $k$-space [14]. The infinitesimal $d\vec{k}$ can further be split into a constant-energy surface element

$df_E$ and a component $dk_\perp$ normal to it i.e. $d\vec{k} = df_E dk_\perp$. Hence, the energy-infinitesimal becomes the gradient of the energy multiplied with the parallel $k$-vector: $dE = |\nabla_{\vec{k}} E| dk_\perp$. Equation 2.5 can thus be written

$$D(E)dE = \frac{1}{(2\pi)^3} \left( \int_{E(\vec{k})=const} \frac{df_E}{|\nabla_{\vec{k}} E|} \right) dE \tag{2.6}$$

where $\frac{1}{(2\pi)^3}$ is the amount of states in $k$-space in one unit volume of the system. At band extrema, the integrand diverges, which are called van't Hove singularities [24].

For free electrons, the DOS can now easily be found by inserting an expression for the unit surface and the gradient of the dispersion relation ($E = \frac{\hbar^2 k^2}{2m^*}$; $m^*$ is the effective mass) into Equation 2.6. The expressions for 1D, 2D and 3D are given in Equation 2.7.

$$\begin{aligned} 3D: \ D(E) &= \frac{1}{(2\pi)^2} \left( \frac{2m^*}{\hbar^2} \right)^{3/2} \sqrt{E} \\ 2D: \ D(E) &= \frac{1}{2\pi} \left( \frac{2m^*}{\hbar^2} \right) \\ 1D: \ D(E) &= \frac{1}{\pi} \left( \frac{2m^*}{\hbar^2} \right) \frac{1}{\sqrt{E}} \end{aligned} \tag{2.7}$$

The shape of the DOS (Figure 2.4) for materials of different dimensionality gives very different behaviour around the band edges. It can be seen that by lowering the dimensionality, the density of states becomes more concentrated, which creates better conditions for higher-efficiency light emitters.

### *2.3.3 Joint DOS*

Transitions proceed from an initial state to a final state. To take this into account the joint DOS is introduced, which defines the density of states separated by a given energy in the vicinity of the bandgap energy $E_g$.

In the parabolic band approximation, valid close to band extrema, the dispersion relation of the CB and VB can be defined as follows:

$$E_c(k) = E_g + \frac{\hbar^2 k^2}{2m_e^*} \tag{2.8}$$

$$E_v(k) = -\frac{\hbar^2 k^2}{2m_h^*} \tag{2.9}$$

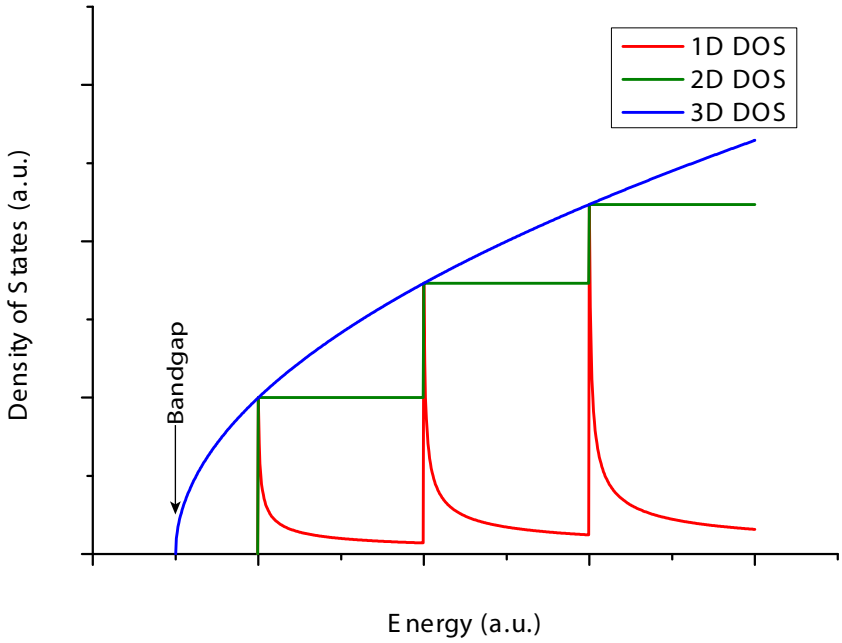


*Fig. 2.4:* Illustration of the joint density of states for one (red), two(green) and three (blue) dimensions. Lower dimensionality gives higher localization, which enhances light-emitting capabilities.

In an optical transition caused by a photon with energy $\hbar\omega$, momentum conservation gives the expression,

$$\hbar\omega = E_c(k) - E_v(k) = E_g + \frac{\hbar^2 k^2}{2\mu}, \tag{2.10}$$

where $\mu = \frac{m_e m_h}{m_e + m_h}$ is the reduced mass. Hence, $k = \frac{1}{\hbar}\sqrt{2\mu(\hbar\omega - E_g)}$, which gives finite values for the joint DOS when $\hbar\omega > E_g$.

$$\begin{aligned} 3D: \;& D(E) = \frac{1}{2\pi^2}\left(\frac{2\mu}{\hbar^2}\right)^{3/2}\sqrt{\hbar\omega - E_g} \\ 2D: \;& D(E) = \frac{1}{2\pi}\left(\frac{2\mu}{\hbar^2}\right) \\ 1D: \;& D(E) = \frac{1}{\pi}\left(\frac{2\mu}{\hbar^2}\right)\frac{1}{\sqrt{\hbar\omega - E_g}} \end{aligned} \tag{2.11}$$

### *2.3.4 Carrier Stastistics*

Particles may be classified according to their spin, which can take integer and non-integer values. Indistinguishable quantum-mechanical particles and quasiparticles with integer spin are called *bosons* and follow Bose-Einstein statistics. To describe the statistics of non-integer spin particles, called *fermions*, the Fermi-Dirac function is used. Fermions are subject to the *Pauli exclusion principle*, which states that two fermions in the same unit cell are not allowed to occupy the same quantum state i.e. have the same set of quantum numbers. The limit at high temperature and low concentration is, for both functions, the Maxwell-Boltzmann distribution. The three equations mentioned are:

$$f_{MB} = Ae^{E/kT} \tag{2.12}$$

$$f_{BE} = \frac{1}{e^{E/kT} - 1} \tag{2.13}$$

$$f_{FD} = \frac{1}{e^{E - E_F/kT} + 1} \tag{2.14}$$

$E_F$ is the *Fermi level*, which is defined as the energy level at which the occupation probability is 1/2, as can bee seen from the equation. The Fermi level definition is temperature independent and it is hence a function of the temperature, $E_F = E_F(T)$. Other factors which induce changes in carrier concentration e.g. doping concentration, excitation density and surface states, will thus change the Fermi level, as well.

### 2.3.5 Excitons

Excitons are electron-hole pairs bound by Coulomb attraction [25][26]. By absorption of a photon, an electron is excited out of the valence band and into the conduction band. The *hole* left in the valence band i.e. the missing electron, is considered a positively charged particle. The mobility of a hole is intuitively lower than for a free electron and the effective mass is hence larger, both are expressed in terms of values used for a free electron [13]. Upon excitation the electron is attracted to the hole by Coulomb attraction and a neutral excitation particle is formed. The energy gained when a weak bond is formed makes the excitation more energetically favourable and thus enables the material to absorb light at energies below the band gap ($E_g$), as will be explained further in Section 2.4.1.

The situation can also be seen as a decrease in the electron-electron repulsion in the excited state relative to the ground state. This arises from more available orbitals, which decreases the Pauli repulsion between the excited electrons [26]. The energy of the continuum of states in the conduction band is hence lowered corresponding to the exciton binding energy, $E_b = E_g - E_x$, where $E_x$ is the exciton energy.

The excitons are normally free particles moving in the lattice, but may bind to defects if its energetically favourable. The energy gained in the binding process, will further decrease the exciton energy and result in a lower emission energy. However, only free excitons are considered here.

Excitons are classified by the dielectric properties of the material in which they exist [26]. Typically, one divides excitons into two limiting cases: *Frenkel excitons* (low $\varepsilon$) and *Wannier-Mott excitons* (high $\varepsilon$). Special cases like surface excitons and atomic/molecular excitons exist as well, but will not be covered here.

#### *Frenkel excitons*

In materials with small dielectric constants, typically molecular structures, the electron-hole separations in excitons tend to be small because of less screening of the Coulomb interaction. The electronic excitation is delocalized over the subunits (e.g. molecules) of the material, but the electron and hole are together localized on individual subunits [25]. The separation between the subunits is in the range of 5 Å, which gives a negligibly small sharing of electron density i.e. a small wave function overlap. Binding energies for Frenkel excitons lie around 0.1 to 1 eV and photoexcitation will therefore usually not create free charge carriers in these materials. To sep-

arate the charge carriers, dopants which act as electron acceptors typically have to be introduced. This is important for photovoltaic applications [27].

*Mott-Wannier excitons*

In materials with large dielectric constants, usually the case in semiconductors, the electric field screening reduces the Coulomb interaction and the excitons are hence in general larger. Contrary to the case for Frenkel excitons the electronic interaction between the subunits is large for Wannier-Mott excitons and is proportional to the wave function overlap. The fact that the radius of the exciton exceeds the lattice spacing, enables the not continuum-like lattice potential to be incorporated into the effective mass of the electron and hole. The large radius of the Wannier excitons corresponds to a weak bond, usually in the order of 0.01 eV.

The weakly bound (Mott-Wannier) excitons show quantized energy levels described by a modified Rydberg equation [13]. This is observed as absorption and luminescence lines at energies below the band gap. To find a mathematical expression describing this feature, the Hamiltonian of the system is used:

$$H = -\frac{\hbar^2}{2m_e}\nabla_e^2 - \frac{\hbar^2}{2m_h}\nabla_h^2 - \frac{e^2}{4\pi\varepsilon_0\varepsilon|\vec{r}_e - \vec{r}_h|} \tag{2.15}$$

This comprises the kinetic energy of the electron and the hole and the Coulomb attraction between them. Schrödinger's time-independent equation,

$$H\Psi(\vec{r}_e, \vec{r}_h) = E'\Psi(\vec{r}_e, \vec{r}_h), \tag{2.16}$$

needs to be solved to find the energetic behaviour of the exciton particle. To ease the calculations, a center-of-mass coordinate system is introduced: $\vec{R} = \frac{1}{\mu}(m_e\vec{r}_e + m_h\vec{r}_h)$ and $\vec{\rho} = \vec{r}_e - \vec{r}_h$. Schrödinger's equation then becomes,

$$\left[-\frac{\hbar^2}{2M}\nabla_R^2 - \frac{\hbar^2}{2\mu}\nabla_\rho^2 - \frac{e^2}{4\pi\varepsilon_0\varepsilon_r\rho}\right]\Psi = E'\Psi, \tag{2.17}$$

where $M = m_e + m_h$ and $\mu = m_e m_h/M$ are the total and reduced mass, respectively. This is solved by the method of separation of variables, $\Psi(\vec{R,\rho}) = \psi(\vec{R})\varphi(\vec{\rho})$. Equation 2.17 may then be written,

$$\underbrace{-\frac{\hbar^2}{2M\psi}\nabla_R^2\psi}_{-W} \underbrace{-\frac{1}{\varphi}\left[\frac{\hbar^2}{2\mu}\nabla_\rho^2\varphi + \frac{e^2\varphi}{4\pi\varepsilon_0\varepsilon_r\rho}\right]}_{-E} = E'. \tag{2.18}$$

Simplifying this to $W + E = E'$, enables the decoupling of this equation into the center of mass motion and the relative motion of the electron and hole. The two equations become,

$$\nabla_R^2 \psi + k^2 \psi = 0 \tag{2.19}$$

$$\left[ \frac{\hbar^2}{2\mu} \nabla^2 + \frac{e^2}{4\pi\varepsilon_0 \varepsilon \rho} \right] \varphi = -E\varphi, \tag{2.20}$$

where $k^2 = \frac{2MW}{\hbar^2}$. The first equation (Eq. 2.19) has the plane wave solution $\psi(R) = Ae^{i\vec{k}\vec{R}}$, which describes a free particle moving through the material. It follows that the translational motion energy is $W = \frac{\hbar^2 k^2}{2M} = \frac{p^2}{2M}$.

The second equation (Eq. 2.20) is as anticipated, the Schrödinger equation for the hydrogen atom, one of few systems which can be solved analytically. The solution is,

$$E_n = -\frac{\mu e^4}{32\pi^2 \hbar^2 \varepsilon_0^2 \varepsilon_r n^2}, \tag{2.21}$$

where $\mu$ is the reduced mass, $n$ is the quantum number and $\varepsilon$ is the effective dielectric permittivity. In the limit of high n's this formula converges towards free carriers, where the thermal energy exceeds the exciton binding energy. It is often written as $E_n = -\frac{E_b}{n^2}$, where $E_b = \frac{\mu}{m\varepsilon_r^2} \times 13.6eV$. The energy of the bound electron-hole pair i.e. the exciton can thus be written,

$$E_x' = E_g - \frac{E_b}{n^2} + \frac{p^2}{2M}. \tag{2.22}$$

Transitions proceed between the bottom of the CB to the top of the VB. In direct gap materials, this occurs in the center of the Brillouin zone since the carriers reside here to minimize their energy. Also, $\Delta k \approx 0$ for such transitions, which is necessary since photons carry a negligible momentum. The last term in Eq. 2.22 hence becomes negligible.

Binding energies for free excitons in ZB GaAs is ∼4 meV [28]. In WZ higher values are expected, based on a larger electron effective mass in the WZ $\Gamma_{8c}$-band [6], but it has not yet been determined.

### *2.4 Photoluminescence of Nano-sized Semiconductor Materials*

Photoluminescence (PL) spectroscopy is a powerful method to investigate the energetic behaviour of a material. In the field of electronics and semiconductor technology it is a widely used technique to gain further insight

in the structure properties of the material at hand [11]. Its non-destructive character and high sensitivity enables characterization of organic and inorganic materials where surface properties are of interest. PL measurements give information about the electronic structure and optical properties and show its strengths in exploring defects, charge carrier trapping and mobility.

A general introduction to photoluminescence is first presented, before the physical mechanisms are described with Fermi's rule.

### *2.4.1 Photoluminescence mechanism*

Incoming photons with energy $h\nu \geq E_g$ are absorbed in which one photon supply the energy to excite one electron to the CB. This also works the other way around; an incoming photon can induce the emission of another photon with the exact same frequency and phase, giving two equal photons. The stimulated emission will hence grow exponentially as long as there are CB electrons which can supply the energy by relaxing into the VB [29]. This is important in most lasers, where a population inversion i.e. more electrons in the CB than in the VB, is needed to make stimulated emission more probable than absorption. In PL however, the information is extracted from spontaneous emission, where recombination is described by a probability function, such as Fermi's golden rule (Sec. 2.4.2).

Figure 2.5 shows an illustration of the photophysical processes of a semiconductor excited by light higher than the bandgap. The red arrows represent processes were light is either emitted or absorbed, the white arrows are non-radiative processes. The different processes are:

(I) The photo-excitation where an electron is promoted from the VB to the CB, whereby a hole is simultaneously created in the VB. If $h\nu > E_g$ the electron will quickly relax to the CB bottom through e-e and e-phonon scattering. This phase relaxation happens in the range of a few femtoseconds (fs).

(II) In the band-band PL an electron relaxes from the CB edge to the VB edge, recombining with a hole and releasing the energy difference as a photon.

(III) Transitions which gives PL with $h\nu < E_g$ from sub-band states are possible from both excitonic states (Sec. 2.3.5), and from defects and surface states.

(IV) Solely non-radiative decay is also a possibility and can happen directly

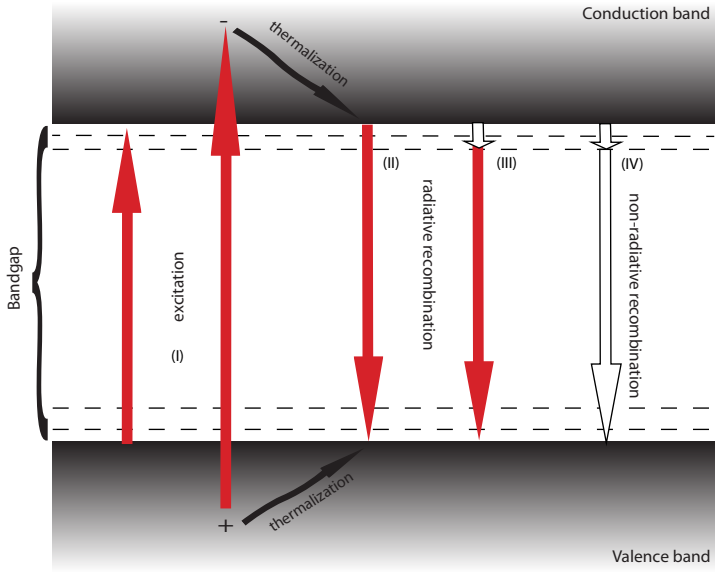


*Fig. 2.5:* Generalization of the processes associated with optical excitation of a material. Red arrows represent radiative transitions, while white arrows shows non-radiative processes. Process (I) shows excitation of electrons to the conduction band or above. Radiative recombination may proceed as a band-band transition (II) or from sub-band states (III). (IV) represents non-radiative recombination.

or indirectly (in figure). This process is significantly increased by defects and impurities.

Transition II and III are the processes which create the PL signal. The relative signal reflects the efficiency of the two mechanisms. The intensity of the signal with the band-band energy indicates the rate at which direct recombination occurs, while the signal from different sub-band levels indicates the concentration of different defect sites. By introducing new relaxation routes to excited electrons, the population will decay faster than in a stringent two-level system. Time-resolved measurements can reveal the efficiencies of such processes.

### 2.4.2 Fermi's Golden Rule

To describe light-matter interaction, Fermi's Golden Rule is derived in this section. The goal is expressions concerning electronic transitions in a solid, in connection with absorption and emission of light. The derivation makes use of a quantum mechanical approach, including perturbation theory. First, a single atom atom is considered, and the result is modified to apply for solids subsequently.

The quantum mechanical approach makes use of the time-dependent Schrödinger equation,

$$i\hbar\delta_t\Psi = \hat{H}\Psi. \tag{2.23}$$

The incident electromagnetic field results in a harmonic perturbation ($V_1$) to the Hamiltonian,

$$\hat{H} = \hat{H}_0 + \lambda\hat{V}_1, \tag{2.24}$$

where $V_1 = \vec{p}\vec{E}$. $\vec{p}$ represents the transition dipole moment and $\vec{E} = \vec{E}e^{i\omega t} + \vec{E}^* e^{i\omega t}$ is the time-varying electric field. The electric field is considered to have a small influence on the system i.e. a small deviation from a system in the absence of an electric field. The perturbed wave function can then be written as a sum of different orders of "smallness",

$$\Psi = \Psi^{(0)} + \lambda\Psi^{(1)} + \lambda^2\Psi^{(2)} + ... \tag{2.25}$$

The perturbed functions are substituted into Eq. 2.23 and the terms of equal order are equated, which gives, in the zeroth, first and second approximation,

$$\begin{aligned} 0^{th}\ order:&\ \ i\hbar\delta_t\Psi^{(0)} - \hat{H}\Psi^{(0)} = 0 \\ 1^{st}\ order:&\ \ i\hbar\delta_t\Psi^{(1)} - \hat{H}\Psi^{(1)} = V_1\Psi^{(0)} \\ 2^{nd}\ order:&\ \ i\hbar\delta_t\Psi^{(2)} - \hat{H}\Psi^{(2)} = V_1\Psi^{(1)} \end{aligned} \tag{2.26}$$

From the solution of the zeroth order equation, the accuracy can be increased by stepwise involving higher order solutions. Therefore, the complete solution becomes the sum of the wave functions.

$$\Psi = \lim_{\lambda\to 1}\left\{\psi^{(0)} + \lambda\psi^{(1)} + \lambda^2\psi^{(2)} + ... + \lambda^n\psi^{(n)}\right\} \tag{2.27}$$

The first order equation, written as the Schrödinger equation for a single particle moving in an electric field, can now be written,

$$\left[i\hbar\delta_t + \frac{\hbar^2}{2m}\nabla^2 - V\right]\Psi^{(1)} = V_1\Psi^{(0)}. \tag{2.28}$$

For the zeroth order (unperturbed system) the solution is $\Psi^{(0)} = \psi_{E_i} e^{-\frac{i}{\hbar}E_i t}$, where $\psi_{E_i}$ is assumed known. These wave functions form a complete set for all possible $i$'s, and $\Psi^{(1)}$ can thus always be expanded in the following way:

$$\Psi_i^{(1)} = \sum C_{ij}^{(1)} \psi_{E_j} e^{-\frac{i}{\hbar}E_j t} \tag{2.29}$$

This equation is inserted into Equation 2.28, multiplied with the complex conjugate of $\Psi_{E_j}$ and the result integrated in space:

$$i\hbar\delta_t C_{ij}^{(1)} = \int \psi_{E_j}^* V_1 \psi_{E_i} e^{\frac{i}{\hbar}(E_j - E_i)t} d^3x \tag{2.30}$$

Rearranged and integrated over time, the expression becomes,

$$C_{ij}^{(1)} = -\frac{i}{\hbar} \int \left[ \int \psi_{E_j}^* V_1 \psi_{E_i} d^3x \right] e^{\frac{i}{\hbar}(E_j - E_i)t} dt \tag{2.31}$$

The term in the square brackets can (with $V_1 = \vec{p}\vec{E}$) be written,

$$\int \psi_{E_j}^* V_1 \psi_{E_i} d^3x = e z_{ij} E_z, \tag{2.32}$$

where

$$z_{ij} = \int \psi_{z_j}^* p_z \psi_{z_i} d^3x \tag{2.33}$$

are the dipole matrix elements. Symmetry considerations reveal allowed/non-allowed transitions i.e. the selection rules. These depend on crystal symmetry and hence on band symmetry, as will be explained in Sec. 2.2.2. If the integrand in Eq. 2.33 is an odd function, the transition is not allowed, whereas even integrands give allowed transitions.

Further, with $\omega_{ji} = \frac{1}{\hbar}(E_j - E_i)$ Eq. 2.31 becomes,

$$C_{ij}^{(1)} = \frac{e z_{ij} E_z \left(1 - e^{i(\omega_{ji} - \omega)t}\right)}{\hbar(\omega_{ji} - \omega)} + \frac{e z_{ij} E_z \left(1 - e^{i(\omega_{ji} + \omega)t}\right)}{\hbar(\omega_{ji} + \omega)}. \tag{2.34}$$

At resonance ($\omega_{ji} \simeq \omega$) the second part becomes negligible. The total wavefunction of the system is $\Psi(\vec{r}, t) = \psi_{E_i} e^{-\frac{i}{\hbar}E_i t} + \sum_{i \neq j} C_{ij}^{(1)} \psi_{E_i} e^{-\frac{i}{\hbar}E_i t}$, where the first term describes the initial state. Interaction with an electromagnetic field may cause a transition and leave the system in a different state. The probability of this is expressed as the square of the wavefunction. The $\psi_{E_i}$'s are orthogonal and one can hence square Equation 2.34 to find the probability of the transition.

$$\left| C_{ij}^{(1)} \right|^2 = \frac{e^2}{\hbar^2} |z_{ji}|^2 |E_z|^2 \frac{2[1 - \cos(\omega_{ji} - \omega)t]}{(\omega_{ji} - \omega)^2} \tag{2.35}$$

The transition rates ($W_{ij}$) are then found by taking the time-derivative of this function:

$$W_{ij} = \frac{\delta}{\delta t}\left|C_{ij}^{(1)}\right|^2 = \frac{2e^2}{\hbar^2}\left|z_{ji}\right|^2\left|E_z\right|^2\frac{\sin(\omega_{ji}-\omega)t}{(\omega_{ji}-\omega)} \tag{2.36}$$

For a slow perturbation ($t \to \infty$) the last factor becomes the delta function. This gives Fermi's golden rule for an isolated atom:

$$W_{ij} = \frac{2\pi e^2}{\hbar^2}\left|z_{ji}\right|^2\left|E_z\right|^2\delta(\omega_{ji}-\omega) \tag{2.37}$$

The transition rates hence depend on the selection rules ($|z_{ij}|^2$), the electromagnetic field ($|E_z|^2$) and the density of states which is a delta function in an atom.

In semiconductors, the continuum of states below and above the VB and CB, respectively, alters the solution found in Section 2.4.2. An electron transition from $E_i$ to $E_j$ will be multiplied with $f_{FD}(E_i)[1 - f_{FD}(E_j)]$. Since $f_{FD}$ is the Fermi-Dirac distribution, this represents the distribution states in the VB and CB. All the possible combinations where absorption is possible is now described by the joint density of states ($D(\omega_g - \omega)$, rather than by the delta function. The equations for absorption and emission become,

$$W_{VB-CB} = \frac{2\pi e^2}{\hbar^2}\left|z_{ji}\right|^2\left|E_z\right|^2 D(\omega_g-\omega)f_{FD}(E_{VB})[1-f_{FD}(E_{CB})] \tag{2.38}$$

$$W_{CB-VB} = \frac{2\pi e^2}{\hbar^2}\left|z_{ji}\right|^2\left|E_z\right|^2 D(\omega_g-\omega)[1-f_{FD}(E_{VB})]f_{FD}(E_{CB}), \tag{2.39}$$

respectively. If $E_z$ in Eq. 2.39 is the same as in Eq. 2.38, the former gives the rate of stimulated emission. In direct-gap materials, the $|z_{ij}|^2$ factor will, in addition to the selection rules, maintain the momentum conservation requirement. With these equations the light-matter interaction can be better understood and measurement results can be interpreted and anticipated.

A simplified band structure in the Brilluoin zone center, with allowed transitions based band symmetry, is shown in Fig. 2.6. Both [6] and [10] agree on this valence band structure, the selection rules are taken from the latter. As can be seen in Fig. 2.1, the $\Gamma_{9V}$-band has a heavy-hole character, while topmost $\Gamma_7$-band is the light-hole band. The lower $\Gamma_7$-band is the split-off band. The lowest-energy exciton is measured to 1.517 eV in [10].

In Section 2.4.1 basic introduction to the mechanisms governing PL were presented. After the derivation of the equations concerning this topic in this section, a more thorough treatment of absorption and emission now follows. This is done in the framework of the above discussion.

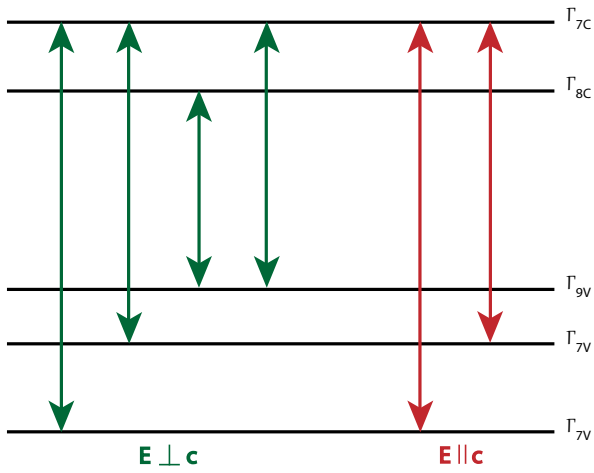


*Fig. 2.6:* Band structure at the Γ-point for WZ GaAs. The arrows show allowed perpendicular (green) and parallel (red) transitions. From the highest valence band, only perpendicular transitions are allowed.

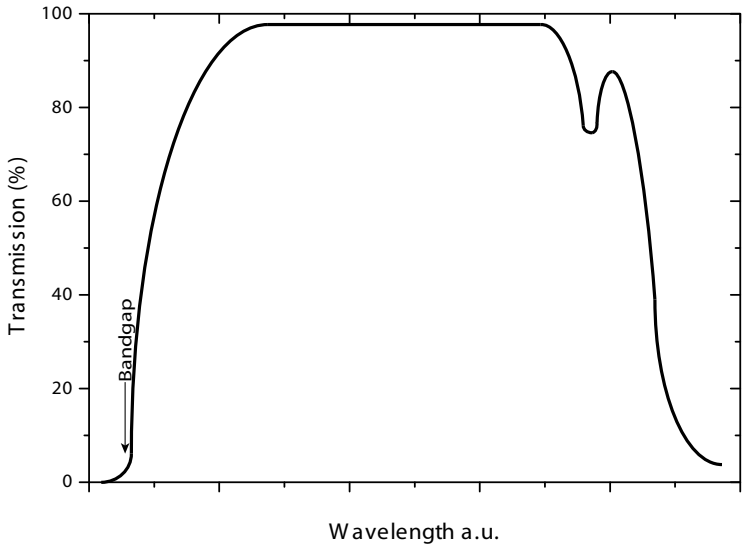


*Fig. 2.7:* Generalized transmission spectrum. Absorption can be seen at low wavelengths above the bandgap, and at high wavelengths, where phonons are excited.

### *Absorption*

As can be seen from Eq. 2.38, a photon with $E \geqslant \hbar\omega$ can excite an electron from the VB to the CB. Initially, the VB is considered occupied by electrons and the CB almost empty. This results in a broad range of frequencies where absorption is allowed, which can be seen in the absorption spectrum. At the bandgap energy a near step-like shape is observed, above which absorption is possible. The effect on transmission can be seen in Fig. 2.7. The roundness of the absorption edge is called the Urbach tail, and is believed to arise from DOS features. Absorption is also seen at higher wavelengths where excitation of optical phonons are present.

### *Luminescence*

The type of luminescence is defined by how the material is excited. In addition to photoluminescence (PL), as worked with here, other techniques exist e.g. cathodoluminescence, electroluminescence and chemiluminescence.

Intuitively, absorption and emission can be seen as reverse processes, which to some degree holds true. There are however differences that can be

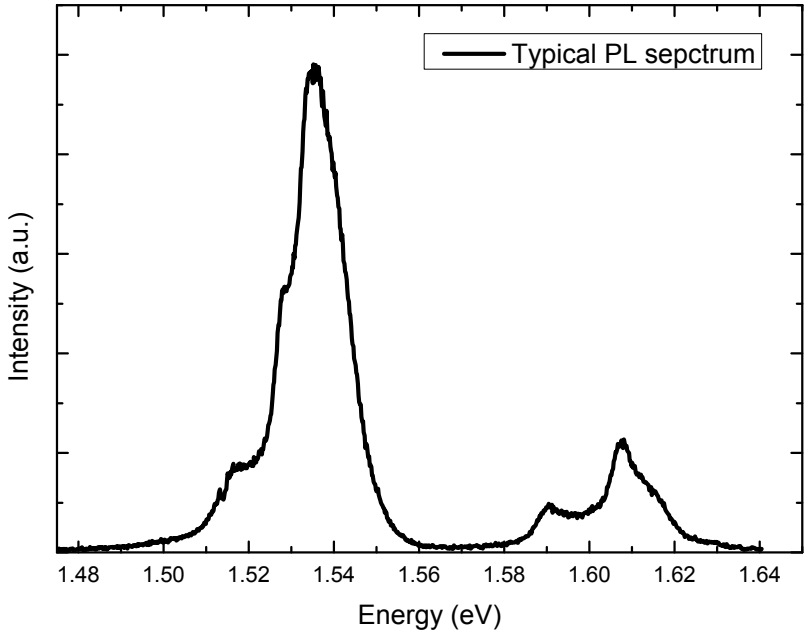


*Fig. 2.8:* Measured PL spectrum of an AlGaAs NW with a GaAs insert at 8.6K. Two sets of sharp peaks appear from the two materials.

understood in the light of the equations in Fermi's Golden Rule (Eq. 2.39 and 2.38), more specifically the population factor. Whereas a broad range of transitions are available for absorption of light, the emission happens mostly from states in close vicinity to the band edges. The reason for this is that excited charge carriers relax to the band edges non-radiatively after excitation, through interaction with phonons. This happens on the *femtosecond*-scale and is hence seen as instantaneous compared to the lifetime of radiative states. Because of the thermalization of charge carriers to the band edges, the Fermi-Dirac functions of Eq. 2.39 become sharp peaked. Thus, the recombination gives radiation in a narrow range, which explains the sharp peaks observed. An example of this is shown in Fig. 2.8.

Because of the narrow emission lines, PL measurements are extremely sensitive to defects in a material. The defects may introduce new energy levels, which can be resolved as small peaks in the PL spectra.

### 2.4.3 Photoluminescence of quantum confined materials

In a material of reduced dimensionality the charge carriers are spatially confined in one or more directions. This alters the properties of the material and introduces qualitatively new effects. This section treats quantum confinement in semiconductors related to PL spectroscopy.

#### *Effect on the Bandgap*

One of the elements that changes subject to quantum confinement is the bandgap, as was mentioned when treating stacking faults in GaAs NWs (Sec. 2.2.1). Fig. 2.2 showed charge carriers confined in potential wells, where discrete energy levels appeared which were raised with respect to the band edge. Analytical solutions for finite depth wells are not possible, but the solution for infinite potential confinement gives a good basis for a qualitative analysis:

$$E_n = \frac{\pi^2 n^2 \hbar^2}{2md^2} \tag{2.40}$$

Quantum confinement appears when the spatial dimensions are smaller than 2-3 Bohr radii. This constraint applies in the confined directions of the material i.e. charge carriers are confined perpendicular to a 2D quantum well. For structures of different dimensions the dispersion relations become:

$$\begin{aligned}
3D : (bulk)\ E(k) &= \frac{\hbar^2 k^2}{2m^*} \\
2D : (quantum\ well)\ E(k) &= \frac{\pi^2 n_x^2 \hbar^2}{2md_x^2} + \frac{\hbar^2(k_y^2 + k_z^2)}{2m^*} \\
1D : (quantum\ wire)\ E(k) &= \frac{\pi^2 n_x^2 \hbar^2}{2md_x^2} + \frac{\pi^2 n_y^2 \hbar^2}{2md_y^2} + \frac{\hbar^2 k_z^2}{2m^*} \\
0D : (quantum\ dot)\ E(k) &= \frac{\pi^2 n^2 \hbar^2}{2md^2};\ n^2 = n_x^2 + n_y^2 + n_z^2
\end{aligned} \tag{2.41}$$

In 3D the dispersion is continuous, while in a quantum dot the energy levels are discrete in all three dimensions. It is also clear that the energy levels represent the onset of a new band (subband) in quantum wells and wires, while in quantum dots they are true discrete levels. In semiconductors, both the VB and CB are confined, which causes the effective bandgap to increase, and quantum confinement can in this way be revealed and quantized.

*Effect on Density of states*

As the emission intensity is dependent on the available states a certain energy i.e. the density of states, the PL signal will be affected by quantum confinement. This was explained in Sec. 2.3.2, as the density of states (DOS) for structures of different dimensionalities was presented. Now the changed band structure in quantum confined materials is taken into account as the implications of the altered DOS is considered.

For bulk semiconductors (SCs) the DOS goes to zero at the band edge (Fig. 2.4). In the quantum confined cases the DOS is largest at the lowest allowed level within the same subband. As explained above, in 2D systems i.e. quantum wells, the density of states is constant in each subband, and increases when a new subband is reached. In quantum wires the DOS is maximum at the band edge and decays exponentially until a new subband is reached. In quantum dots (QD) the DOS is a $\delta$-function, similar to isolated atoms. This yields a significantly enhanced emission efficiency, and is one of the main motivations for miniaturization of light emitters.

As was mentioned in Sec. 2.3.2, the density of states goes to infinity at band extrema, called van't Hove singularities. In 3D, the DOS is not divergent, although the derivative of energy surface is [13] (see Eq. 2.6). However, Fig. 2.4 shows the DOS of 1D systems to diverge at the bottom of each band, which will be reflected in PL measurements.

*Effect on Crystal Symmetry*

Strain or breaking of symmetry may cause energy shifts and lifting of degeneracies in quantum confined materials. Valence bands are often degenerate at $k = 0$, and the bands are then classified according to the effective mass of the holes residing in the bands. In ZB GaAs the VB is doubly degenerate, and the bands are denoted heavy-hole (hh) and light-hole (lh), see Fig. 2.9. In confined systems the degeneracy is lifted, an effect which is measureable in PL. In WZ GaAs, the ll-hh splitting appears also in bulk.

*Effect on Excitons*

Quantum confinement will also affect the spatially extended excitons. To calculate this effect, Eq. 2.22 is first rewritten as,

$$E(n_B, k) = E_g - Ry\frac{1}{n_B^2} + \frac{\hbar^2}{2M}(k_x^2 + k_y^2 + k_z^2). \tag{2.42}$$

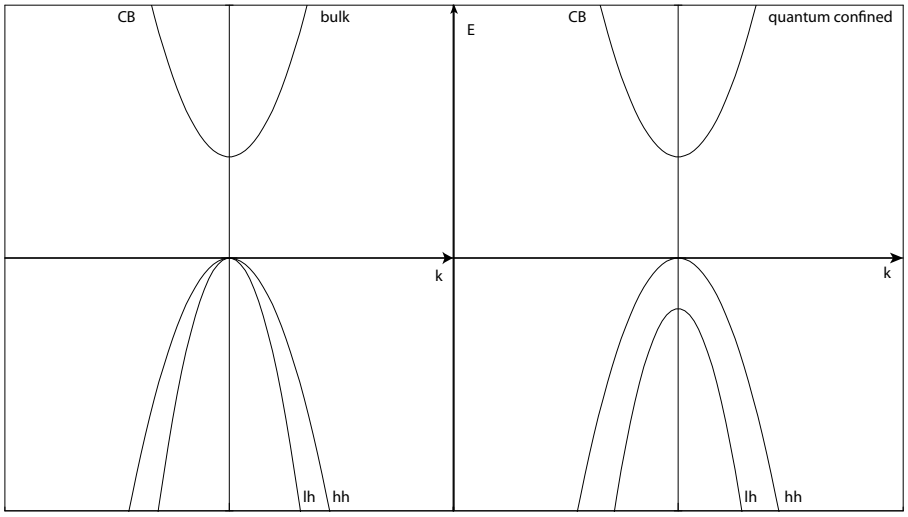


*Fig. 2.9:* Simplified band structure to illustrate lifting of the degenerate valence band in GaAS.

where $Ry = 13.6eV$ is the ionization energy of an exciton in the ground state. Eq. 2.42 describes excitons with continuous momentum in three dimensions i.e. the carriers are free in all directions. In 2D this relation becomes,

$$E(n_B, k) = E_g + E_Q - Ry\frac{1}{(n_B^2 - 1/2)} + \frac{\hbar^2}{2M}(k_x^2 + k_y^2), \tag{2.43}$$

where $E_Q$ is the added electron and hole quantization energy. The exciton binding energy is increased, as well. The Schrödinger equation on the following form is used to quantify this effect:

$$-\frac{\hbar^2}{2m}(\frac{\delta^2\Psi}{\delta x^2} + \frac{\delta^2\Psi}{\delta y^2}) - \frac{e^2}{4\pi\varepsilon_0\varepsilon_r r}\Psi = E\Psi \tag{2.44}$$

In polar coordinates ($r = \sqrt{x^2 + y^2};\ \theta = arctan(x/y)$), this becomes

$$\frac{1}{r}\frac{\delta\Psi}{\delta r} + \frac{\delta^2\Psi}{\delta r^2} + \frac{2m}{\hbar^2}\left(E + \frac{e^2}{4\pi\varepsilon_0\varepsilon_r r}\right)\Psi = 0, \tag{2.45}$$

where the spherical symmetry removes the $\theta$-dependency. The trial solution $\Psi = e^{-r/\lambda}$, gives the 2D Bohr radius

$$\lambda_{2D} = \frac{4\pi\varepsilon_0\varepsilon_r\hbar^2}{2me^2}\ , \tag{2.46}$$

Compared to the 3D Bohr radius,

$$\lambda_{3D} = \frac{4\pi\varepsilon_0\varepsilon_r\hbar^2}{\mu m e^2}, \tag{2.47}$$

it appears that

$$\lambda_{2D} = \frac{\lambda_{3D}}{2}. \tag{2.48}$$

With Eq. 2.21 this gives an exciton binding energy of,

$$E_{2D} = \frac{-4me^4}{32\pi^2} = 4E_{3D}. \tag{2.49}$$

Based one this, one can expect to observe excitonic behaviour at higher temperatures in quantum confined materials.

*Consequences of Quantum confinement in photoluminescence spectra*

In PL spectra, quantum confinement generally appears as a blue shift of the main peak compared to bulk. Also, at higher excitation intensities, higher quantized energy levels are populated, which cause higher energy peaks to appear. This will also be the result of symmetry breaking in strained crystals. Further, the DOS in such systems will enhance the emission efficiency and give sharper peaks, which makes it possible to reveal and quantize the degree of quantum confinement in a PL spectrum.

### *2.4.4 High excitation effects*

The Fermi level was defined in Sec. 2.3.4 as the energy level at which the occupation probability is 1/2, given by the Fermi-Dirac distribution (Eq. 2.12). With high intensity excitation, the electron concentration in the CB can be increased to a point where the Fermi level is raised above the actual band. As the generation of holes in the VB is complementary to electron excitation, the same effect applies. This creates separate Fermi levels for the electron and holes. Under such conditions the material is said to be degenerate.

Electronic transitions can now occur between the two quasi-Fermi levels, as well as the normal band-band transitions. In addition to this, transitions can now happen in other high symmetry points, if the Fermi level exceeds the energy barrier. Due to band folding in WZ (Sec. 2.1), transitions are expected to appear, coming from the L-point in the ZB dispersion [17].

# 3. METHOD

AlGaAs NWs with GaAs insert dispersed on a transmission electron microscopy (TEM)-grid with windows of 50 nm thickness, carved out of the $Si_3N_4$ substrate. Single wires were identified and localized with scanning electron microscopy (SEM). This method is meant to enable structural characterization with high resolution (HR)-TEM. Excitation was done with a diode-pumped solid-state laser (cw) and a mode-locked Ti:Sa (pulsed – for the time-resolved PL measurements). The polarization measurements were done according to the method described in Sec. 3.2. The temperature dependence was measured at fixed temperatures from 10 K up to room temperature. Intensity dependence was examined by measuring spectra at different excitation intensities using an adjustable filter.

## *3.1 Experimental*

A schematic of the optical setup used in this work is presented here is shown schematically in Figure 3.1. A CW 532 nm laser can be used directly or be used as a pump laser for a mode-locked Ti:Sa laser (see Section 3.4.1) with a pulsed output (ps/fs) in the red to infrared range. The latter case is necessary for time-resolved measurements. Flip mirrors (marked "f") are used to switch between the excitation/detection options.

The laser beam is focused on the sample with an objective (0.65 NA, 50x, infinity-corrected, NIR, brand name: Mitutoyo) with a focus spot of $\sim$1.5 $\mu$m, sufficient to excite only single wires. To monitor the excited area on the sample, a white light source and a camera can be inserted in the detection path, which enables the laser spot to be aligned on a preselected single NW. Once the right NW is found, the mirror to the camera is flipped out so that the signal may reach the detector. The last mirror can be used to send the signal into the streak camera, through an alternative spectrometer.

The setup includes a Janis ST-500 continuous flow cryostat with a heater, to achieve stable temperatures from 4.4 K up to room temperature. Excitation was done with a Spectra-Physics Millenia Pro s-Series laser,

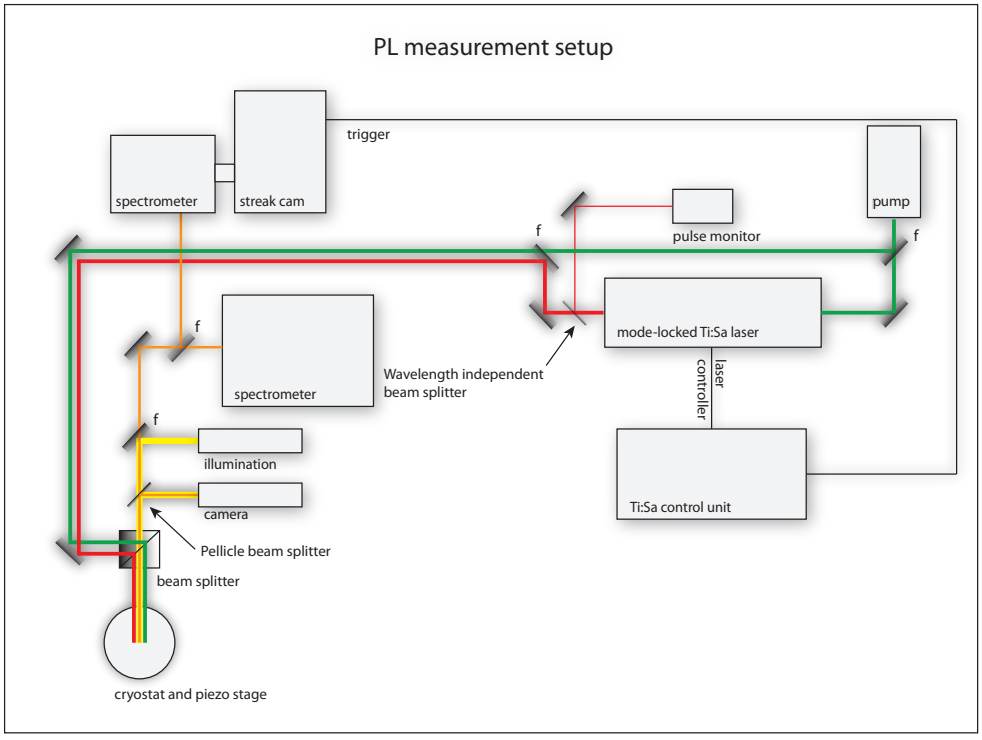


*Fig. 3.1:* Measurement setup for PL. A mode-locked Ti:Sa laser is pumped by a solid-state diode laser (532 nm), which can be used directly, as well. The pulsed IR beam is used for time-resolved measurements. The PL signal is directed towards a spectrometer or a streak-camera (flip mirror). To orientate on the sample white light illumination and a camera can be flipped into place. Flip mirrors are marked "f".

which is a diode pumped frequency doubled continuous wave laser operating at 532 nm. For time-resolved measurement, this laser was used to pump a Spectra-Physics Tsunami mode-locked Ti:Sa laser, with a pulsed output of 2 ps at 80 MHz in the range 700 nm - 1 $\mu$m. The detection setup consisted of a Horiba Jobin Yvon iHR500 spectrometer, with a Peltier cooled CCD (Andor Newton) mounted to its exit slit. A spectral resolution of around 200 meV is expected. For time-resolved measurements, the beam was directed into a Princeton Optics Acton SP2500 spectrometer, in front of an Optronis Optoscope SC-10 streak camera with a temporal resolution of $\sim$2 ps.

## *3.2 Polarization-resolved Photoluminescence*

A material's absorption and emission characteristics depend on the crystal structure, described by Fermi's rule in Section 2.4.2. Hence, one can gain insight in the structure of a material by examining its absorption and emission spectra. This section will first give an introduction to interaction between polarized light and matter, and will then explain the setup used in these measurements, the analysis method and the practical measurement procedure.

### *3.2.1 Introduction to polarization optics*

Light propagates as a transverse wave in free space. The electric and magnetic field form a right-handed triplet with the wavevector, $\vec{k}$ (direction of propagation). The polarization direction is defined by the oscillation orientation of the electric field. In the simplest case, this can be expressed as $\vec{E} = \vec{\epsilon} E_0$, where $\epsilon$ is a constant vector. The electric field is now confined in the plane defined by $\vec{k}$ and $\vec{\epsilon}$, and is called linearly polarized light.

The superposition of two monochromatic waves of different linear polarization can be written,

$$\vec{E}(\vec{x}, t) = [\vec{\epsilon} E_0 + \vec{\epsilon}' E_0'] e^{i(\vec{k}x - \omega t)}. \tag{3.1}$$

Hence, if the wave propagates along $O_z$, the field components are,

$$\begin{aligned} E_x &= a_1 \cos(\vec{k}x - \omega t + \delta_x) \\ E_y &= a_2 \cos(\vec{k}x - \omega t + \delta_y) \\ E_z &= 0 \end{aligned} \tag{3.2}$$

where $\delta_x$ and $\delta_y$ account for the phase shift between the two waves. The non-zero components of the electric field can, with $\vec{k}x - \omega t = \tau$, be written,

$$\frac{E_x}{a_1} = \cos\tau\cos\delta_x - \sin\tau\sin\delta_x \tag{3.3}$$

$$\frac{E_y}{a_2} = \cos\tau\cos\delta_y - \sin\tau\sin\delta_y, \tag{3.4}$$

which again can be combined into,

$$\frac{E_x}{a_1}\sin\delta_y - \frac{E_y}{a_2}\sin\delta_x = \cos\tau\sin(\delta_y - \delta_x) \tag{3.5}$$

$$\frac{E_x}{a_1}\cos\delta_y - \frac{E_y}{a_2}\cos\delta_x = \sin\tau\sin(\delta_y - \delta_x) \tag{3.6}$$

Taking the square of these equations and adding them together (with $\delta = \delta_y - \delta_x$), leaves the equation of an ellipse:

$$\left(\frac{E_x}{a_1}\right)^2 + \left(\frac{E_y}{a_2}\right)^2 - 2\left(\frac{E_x}{a_1}\right)\left(\frac{E_y}{a_2}\right)\cos\delta = \sin^2\delta \tag{3.7}$$

In a plane normal to the direction of propagation, the electric field vector hence describes an ellipse. This is the most general case and is called elliptical polarization. With $\delta$=0, Eq. 3.7 describes linear polarization; if $\delta = \pi/2$, it describes light of circular polarization. The degree of linear polarization is found by,

$$P = \frac{I_{max} - I_{min}}{I_{max} + I_{min}}, \tag{3.8}$$

where the maximum and minimum intensity ($I = |E|^2$) in any direction is measured.

In the Jones formalism the polarization of light can be described with a two-component vector:

$$\vec{E} = \begin{bmatrix} E_x \\ E_y \end{bmatrix} = \begin{bmatrix} E_{0x}e^{i\delta_x} \\ E_{0y}e^{i\delta_y}. \end{bmatrix} \tag{3.9}$$

The electric fields are complex quantities and the intensity is therefore written

$$\vec{I} = \vec{E}^* \cdot \vec{E}, \tag{3.10}$$

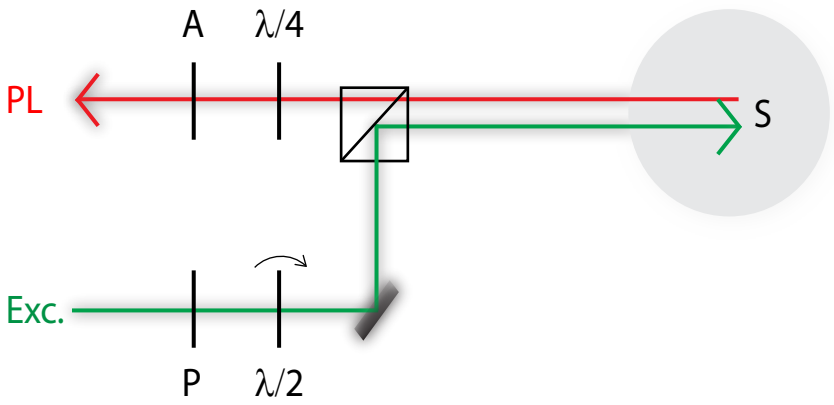


*Fig. 3.2:* A schematic overview of the optical components used for LP measurements. The polarizer (P) ensures linear polarized light, which angle can be controlled with the $\lambda/2$-plate. The analyser (A) is set to maximize the signal, which occurs when the light is polarized along the grooves in the spectrometer. To remove the effect of emission polarization, the $\lambda/4$-plate creates circularly polarized light.

and is in general normalized. The Jones formalism describes the effect of optical elements on polarization with matrices e.g. rotation of a linearly polarized beam along $O_y$ is expressed as

$$\vec{E}_{sample} = \hat{R}(-C)\hat{C}\hat{R}(C)\begin{bmatrix}0\\1\end{bmatrix}, \tag{3.11}$$

where

$$\hat{R}(\alpha) = \begin{bmatrix} cos\ \alpha & sin\ \alpha \\ -sin\ \alpha & cos\ \alpha \end{bmatrix}, \tag{3.12}$$

describes the rotation of an angle $\alpha$. For a $\lambda/2$-plate which is used to rotate the polarization, the $\hat{C}$-matrix is

$$\hat{C} = \begin{bmatrix}1 & 0\\0 & -1\end{bmatrix}. \tag{3.13}$$

### *3.2.2 Excitation with light of variable linear polarization*

To determine the orientation of the nanowire (NW) on the substrate, the setup showed in Fig. 3.2 was used. The polarizer ensures a linear polarized

beam which direction is controlled with the $\lambda/2$-plate. In this way, the direction of polarization of the excitation beam can be scanned over all inequivalent orientations.

When the energy of the excitation beam greatly exceeds the bandgap, the abundancy of available transitions makes absorption independent of selection rules. Because of the dielectric effect, light absorption hence only depends on the angle between the polarized beam and the NW [30]. When the beam is polarized along the NW axis, the absorption is optimal, whereas a minimum is observed when they are perpendicular. Since the emission intensity clearly is dependent on how much light is absorbed, the orientation of the NW can be deduced from the PL signal.

Emission proceeds as band-band transitions, where selection rules apply. This effect is countered in the detection path, which consists of a $\lambda/4$-plate and an analyser. The latter is always set at 90°, which lets light polarized along the grooves of the spectrometer grating through. The $\lambda/4$-plate changes linearly polarized light to circular and will therefore maximize the throughput for all polarizations.

*Excitation polarization in the Jones formalism*

In the following discussion, all angles are defined in a coordinate system where $O_x$ is parallel and $O_y$ is perpendicular to the optical table, when looking along the beam propagation. Positive angles are measured counter-clockwise from $O_x$. The vertically polarized beam from the polarizer can then be described by the Jones vector

$$\vec{E}_{in} = \begin{bmatrix} 0 \\ 1 \end{bmatrix}. \tag{3.14}$$

With Eq. 3.11, the angle (C) of the $\lambda/2$-plate (also called a compensator) then changes the incident beam according to

$$\begin{bmatrix} E_{sample,x} \\ E_{sample,y} \end{bmatrix} = \begin{bmatrix} cos\ C & -sin\ C \\ sin\ C & cos\ C \end{bmatrix} \begin{bmatrix} 1 & 0 \\ 0 & -1 \end{bmatrix} \begin{bmatrix} cos\ C & sin\ C \\ -sin\ C & cos\ C \end{bmatrix} \begin{bmatrix} 0 \\ 1 \end{bmatrix} \tag{3.15}$$
$$\begin{bmatrix} cos^2\ C - sin^2\ C & 2sin\ C\ cos\ C \\ 2sin\ C\ cos\ C & sin^2\ C - cos^2\ C \end{bmatrix} \begin{bmatrix} 0 \\ 1 \end{bmatrix} = \begin{bmatrix} sin\ 2C \\ -cos\ 2C \end{bmatrix}.$$

If now the NW is oriented at an angle $\alpha$ to the x-axis, Equation 3.16 can be used to express the field in the NW coordinate system i.e. $\parallel$ and $\perp$ to the NW orientation.

$$\begin{bmatrix} E_{\parallel\ NW} \\ E_{\perp\ NW} \end{bmatrix} = \begin{bmatrix} cos\ C & sin\ C \\ -sin\ C & cos\ C \end{bmatrix} \begin{bmatrix} sin\ 2C \\ -cos\ 2C \end{bmatrix} = \begin{bmatrix} sin(2C - \alpha) \\ -cos(2C - \alpha) \end{bmatrix} \tag{3.16}$$

Absorption of light perpendicular to the NW is neglected due to the dielectric mismatch effect [31] and the PL intensity should thus be proportional to $E^2_{\parallel\, NW}$:

$$I \propto sin^2(2C - \alpha) \tag{3.17}$$

*Procedure for finding the nanowire orientation*

With the setup described in Section 3.2.2 PL spectra are measured at angles $C \in [0°; 100°]$ with 5° steps. In fact, the interval $[0°; 90°]$ covers all inequivalent angles; two extra steps are carried out to get an overlap. This serves as an alignment check since the PL signal at e.g. 10° and 100° should be equivalent. The 21 spectra obtained are loaded into MATLAB and a 21x1600 matrix is assembled (1600 wavelength points). To visualize the polarization dependency, this matrix can be plotted on a intensity dependent color scale.

Each of the 21 specra is then curve fitted with a set of Lorentzian and/or Gaussian functions. These functions, and the experimental peak, are then numerically integrated. The result is a set of integrated intensities corresponding to a set of compensator positions ($C$). The aim of the measurement is to find the NW orientation ($\alpha$), which is done by least-square fitting of the integrated intensities as a function of compensator position, with Equation 3.17. Since the detection path is left unchanged in this measurement, all peaks should yield similar values of $\alpha$ — independent of its polarization.

### *3.2.3 Analyzing the emission polarization*

When the orientation of the NW is known, the emission polarizations can be analyzed and interpreted. Through the selection rules, deductions of the crystal structure can be made.

A schematic of the setup for this measurement is shown in Figure 3.3. Just as in Section 3.2.2, a polarizer (P) is used to ensure a linear polarized laser beam, perpendicular to the optical table i.e. along $O_y$. The $\lambda/2$- and $\lambda/4$-plates are adjusted to create elliptically polarized light, which after the beam splitter should be circular. The positions of the wave plates which satisfies this requirement is found by inserting a second $\lambda/2$-plate (analyzer) after the beam splitter followed by a power meter. When the beam has a circular polarization, the measured intensity should remain constant while turning the analyzer. This is formalized with Eq. 3.8, where a value as close to 0 as possible is wanted. The circularly polarized beam ensures

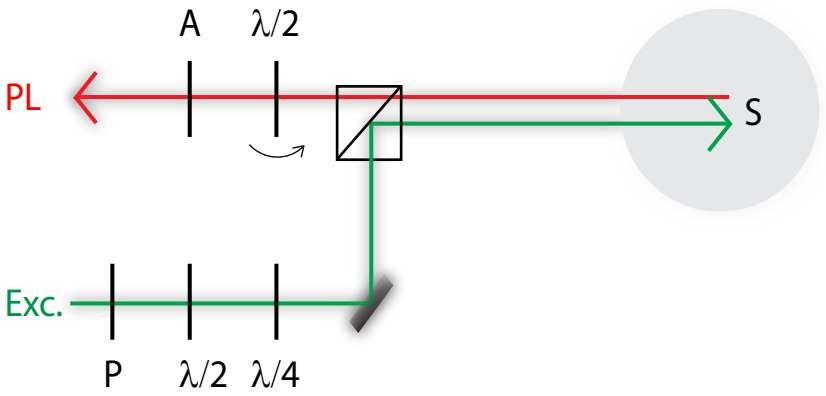


*Fig. 3.3:* A schematic overview of the components used for CP measurements. The polarizer (P) ensures linear polarized light. The following wave-plates are adjusted to give circular polarized excitation. The detection path consists of a $\lambda/2$-plate to rotate the PL polarization. The analyser (A) is again set to maximize the detected signal.

equal excitation conditions for the differently oriented NWs and the crystal axes.

The circular excitation results in emissions with linear polarization dependent on the materials selection rules (see Section 2.4.2). A $\lambda/2$-plate is again used to analyze the beam, and a fixed polarizer is, used to remove detector dependent effects. However, since the system is always considered along the beam propagation direction, $O_x$ in the linear excitation measurement now corresponds to $-O_x$.

*Emission polarization in the Jones formalism*

The unknown polarization of the emission signal is described by Equation 3.18, with the same notation as above.

$$\vec{E}_{sample} = \begin{bmatrix} A \\ B \end{bmatrix} \tag{3.18}$$

which at the spectrometer becomes

$$\vec{E}_{spectrometer} = \underbrace{\begin{bmatrix} 0 & 0 \\ 0 & 1 \end{bmatrix}}_{\hat{A}} \underbrace{\begin{bmatrix} cos\ C & -sin\ C \\ sin\ C & cos\ C \end{bmatrix}}_{\hat{R}(-C)} \underbrace{\begin{bmatrix} 1 & 0 \\ 0 & -1 \end{bmatrix}}_{\hat{C}} \underbrace{\begin{bmatrix} cos\ C & sin\ C \\ -sin\ C & cos\ C \end{bmatrix}}_{\hat{R}(C)} \begin{bmatrix} A \\ B \end{bmatrix}. \tag{3.19}$$

This can further be expressed as

$$\vec{E}_{spectrometer} = \begin{bmatrix} 0 & 0 \\ 0 & 1 \end{bmatrix} \begin{bmatrix} cos\ 2C & sin\ 2C \\ sin\ 2C & -cos\ 2C \end{bmatrix} \begin{bmatrix} A \\ B \end{bmatrix} = \begin{bmatrix} 0 & 0 \\ sin\ 2C & -cos\ 2C \end{bmatrix} \begin{bmatrix} A \\ B \end{bmatrix} \tag{3.20}$$

PL signal polarized at an angle $\alpha$ to $O_x$ can be described by the normalized Jones vector:

$$\begin{bmatrix} A \\ B \end{bmatrix} = \begin{bmatrix} cos\ \alpha \\ sin\ \alpha \end{bmatrix} \tag{3.21}$$

$$\implies \vec{E}_{spectrometer} = \begin{bmatrix} 0 & 0 \\ sin\ 2C & -cos\ 2C \end{bmatrix} \begin{bmatrix} cos\ \alpha \\ sin\ \alpha \end{bmatrix} = \begin{bmatrix} 0 \\ sin(2C - \alpha) \end{bmatrix} \tag{3.22}$$

Hence, with light polarized at an angle $\alpha$ to the x-axis, the PL intensity varies according to $sin^2(2C - \alpha)$ as a function of the compensator position. C is actually varied from 0 to -100° in this model. One must therefore reverse the angles of either the NW orientation or the PL polarization if the two are to be plotted together.

*Procedure for finding the emission polarization*

The simulation and fitting procedure for the polarization determination is the same as for the linear excitation method. The analysis gives a set of angles which describe the polarization of each component of the fitted peaks and the integrated intensity.

As described above, the method starts out with determining the NW orientation to be able to express the emission polarization in the NW coordinate system. As noted earlier, the x-axis is reversed in the detection path, and so are the corresponding angles.

## *3.3 Temperature dependence of material bandgap*

The bandgap energy is known to decrease with increasing energy [32]. There are two mechanisms believed to cause this effect: i) A materials band structure is affected by the crystal potential, which is a sum of contributions

due to electron-electron, electron-core and core-core interactions. The interatomic interaction will change with temperature and hence influence the bandgap. The relative position of the CB and VB i.e. the bandgap, due to the temperature dependent dilation of the lattice is linear at high temperatures and non-linear at low temperature [13]. However, at high temperature, the effect only accounts for a fraction (0.25) of the observed change in bandgap [32]. ii) The relative position of the CB and VB will also be affected by a temperature-dependent electron-phonon interaction.

Empirical models to describe the temperature dependence of the bandgap are used to compare and analyze results [33][32]. Two models are used here, the Varshni model [32] and the modified Varshni as it appears in [33].

$$E_g(T) = E_0 - \alpha T^2(T - \beta) - \text{Varshni model} \tag{3.23}$$

$$E_g(T) = E_0 - \frac{\alpha T^4}{\beta + T^3} - \text{Modified Varshni model} \tag{3.24}$$

### *3.4 Time-resolved photoluminescence*

The temporal response of a material upon excitation with a laser pulse supplies important information on sample properties. A single excitation pulse generates a population of electron-hole pairs which decays through radiative and non-radiative recombination. If a pulse excites $N_x$ excitons, a simple relation describing its decay can be written as a differential equation,

$$\frac{\delta N_x}{\delta t} = -k_{rad}N_x - k_{non-rad}N_x. \tag{3.25}$$

Here, $k_{rad}$ and $k_{non-rad}$ describe the total rate of radiative and non-radiative recombination. These rate constants are functions of several material properties. Impurities and interfaces may introduce new relaxation pathways, which increase the decay rate i.e. decrease the exciton lifetime. These are often non-radiative processes, which therefore limit the lifetimes measured. By considering the exciton population as a function of time $N_x(t)$, Eq. 3.25 can be solved,

$$N_x(t) = e^{-(k_{rad}+k_{non-rad})t} = e^{-t/\tau}, \tag{3.26}$$

where $\tau = 1/(k_{rad} + k_{non-rad})$ is the exciton lifetime. With more than one emitter present, different rate constants appear if the emitters exhibit different lifetimes. In time-resolved PL (TRPL) the signal intensity is measured as a function of time and the resulting curve is curve fitted to Eq. 3.26. A

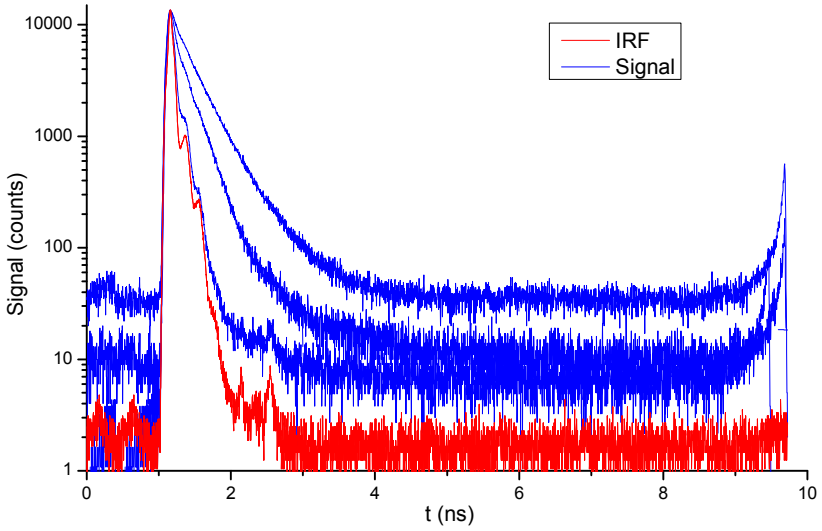


*Fig. 3.4:* Example of a decay curve, showing three different lifetimes. The highest curve corresponds to the slowest decay. The red curve is the instrument response function (IRF), which is the exciting pulse as it is seen by the measurement setup. The fastest is barely measurable as it is almost as fast as the time-resolution of the setup.

muliple-exponential function is needed if there are different emitters in the sample.

Figure 3.4 shows three different decay curves. The logarithmic vertical axis gives straight lines for the exponential-like decays. The exciting pulse (red curve), as it is seen by the measurement setup (instrument response function) is comparable to the fastest decay (lower blue curve). Since this blurs out the time of excitation, the measured lifetimes are affected. To take account for this, a deconvolution step is introduced in the curve fitting procedure. The deconvolution comes from the fact that the measured decay is a convolution of the exciting pulse and the actual decay curve [34]. However, if the pulse width is narrow enough, as it is in this study, the deconvolution step unnecessary. The lifetime is in this case long compared to the pulse width, which can be considered a $\delta$-function.

The lifetime of an excited state depends on its wave function overlap with the relaxed state, since the overlap describes transition probability (see Sec. 2.4.2). Because of this, type II transitions are in general slower because of the spatial electron-hole separation.

Impurities and surface states offer alternative relaxation routes, which

in turn reduces the lifetimes in a material. Both can be seen as to introduce new levels in the bandgap, where non-radiative recombination drains the excited state population.

### *3.4.1 Pulsed Titan:Sapphire Laser*

Unlike a continuous wave (cw) laser, a pulsed laser produces pulses of electromagnetic radiation. The pulses are necessary for time-resolved measurements and can also be needed when one wants high peak energies without producing excessive heat. There are two important factors governing the possible wavelengths in a laser system, the resonator length which determines the longitudinal modes and the range at which the active medium can provide amplification [35]. The resonator length defines the frequencies which can appear as standing waves i.e. the longitudinal modes. Which longitudinal modes that are amplified, depend on the gain-bandwidth of the active medium. The broad bandwidth that solid state lasers typically exhibit is essential for pulsed lasers. The different modes being amplified simultaneously have different phases and will interfere creating a time-varying output. In fact, a broader gain can amplify more modes and thus create shorter pulses.

In a mode-locked laser, the different phases are controlled actively or passively to create a single propagating pulse of radiation. Active mode locking is often done with an *acousto-optic modulator* (AOM) which introduces a loss mechanism operating at the same frequency as the pulse repetition rate, see Figure 3.5. In the AOM standing acoustic waves (rf frequency) are created in a high quality optical material by a piezo-electric transducer. The acoustic waves alter the refractive index of the material and a time-dependent grating is formed. Parts of the light passing through the grating are diffracted and shifted in frequency going both ways through and comprises the loss mechanism, see Figure 3.5a. The grating appears with a frequency of $2\omega_{\mathrm{mL}}$, where $\omega_{\mathrm{mL}}$ is the rf frequency the piezo is driven with. As stated above, this frequency should be set equal to the pulse repetition rate which is $c/2L$, $L$ being the resonator length and $c$ the speed of light. The time-dependent loss leaves sidebands in the frequency domain, as seen in Figure 3.5c, where $\omega$ is the optical frequency. These sidebands are driven in-phase and corresponds to the two adjacent cavity modes. The new in-phase modes are again locked to their adjacent modes until all amplified modes of the active medium and resonator are locked.

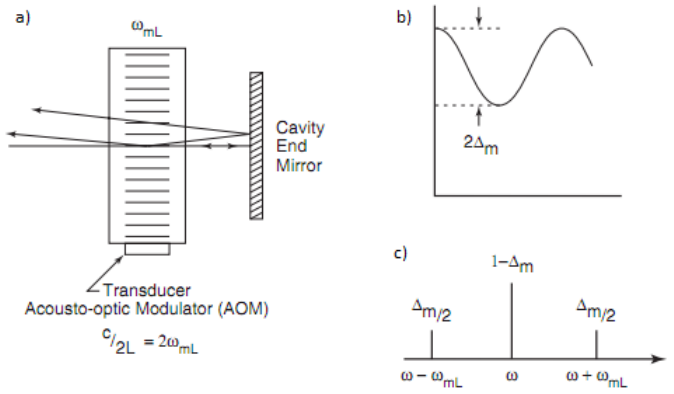


*Fig. 3.5:* Active modelocking using an AOM (a). Modulation sidebands (c) are produced when a wave of frequency $\omega$ passes through an amplitude modulator [35].

### *3.4.2 TRPL detection with a streak camera*

Measurements of the temporal decay can be done with a streak camera, which combined with a spectrometer, enables both temporal and spectral resolution of the PL signal. A schematic can be seen in Fig. 3.6. In front of the entrance slit, a spectrograph disperses the different wavelengths along the horizontal axis. The different wavelengths in the signal pulse, caused by the excitation pulse, therefore hit the the photocathode at different spots.

The photocathode converts light to electrons which are accelerated towards the multi-channel plate (MCP). A triggered sweep voltage, synchronized with the arriving electrons, is applied perpendicular to the line of electrons. Electrons arriving at different times face a different voltage and are consequently deflected at different angles. Hence, the temporal distribution is converted to a spatial distribution along the vertical axis. The MCP amplifies the signal before it hits the phosphor screen, where the signal is converted back to photons which can be imaged with a CCD-camera. The signal intensity is in this way measured both in time and space.

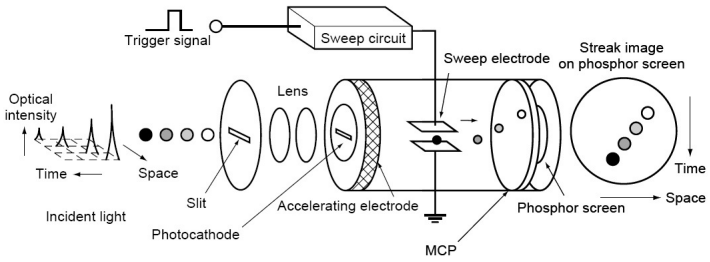


*Fig. 3.6:* Operation principle of a streak camera. A spectrograph has spread out the different wavelengths along the horizontal axis in front of the slit. A photocathode converts the signal to electrons which are deflected at an angle corresponding to their distribution in time. At the MCP the signal is amplified before being converted back to photons by the phosphor screen. A CCD records the intensity on each coordinate (x,y).[reference!]

# 4. RESULTS

Of more than 20 candidate NWs localized with SEM, three were selected for further analysis. These are named NW213, NW221 and NW311, and were among the brightest showing a GaAs peak. NW213 is shown in Fig. 4.1. Intensity dependence, temperature dependence and polarization dependence were investigated for 5 NWs. Results from the two wires not presented will be used to support the argumentation in the discussion.

From the SEM image of NW213 the NW dimensions are estimated to have $l = 2.2$ $\mu$m and d = 120 nm. From the growth conditions, the GaAs inserts are expected to be 110 nm long. The two other wires which were analysed were seen to have similar geometry. NW213 and NW311 had similar shaped tips, which were longer and sharper than for NW221. Other wires had similar lengths or shorter, and had differently shaped tips. It was not achieved to get a measurable PL signal from the NWs without tips. However, no correlation between NW geometry and PL emission was found for the wires with tip.

## *4.1 Temperature*

The wires were measured at fixed temperatures and the spectra normalized to remove any background related artefacts. The peak energies were (least square) curve fitted to the Varshni model (Eq. 3.23) and the modified Varshni model (Eq. 3.24). The spectra were fitted with three Lorentzians to examine the temperature dependence of each emitter. Whereas NW213 is used as a main example, plots of other NWs are shown where needed, to enforce arguments in the discussion.

Figure 4.2 shows normalized spectra, stacked as a function of temperature. The spectra are measured with an excitation intensity 57 kW/cm$^2$, to ensure sufficient signal at high temperatures. At 10 K, the three-Lorentzian fit is indicated with dotted lines. The redshift of around 50 meV is marked with a projection of the modified Varshni model, where the bi-linear y-axis is taken into account. The actual fitted curve can be seen in Fig. 4.3,

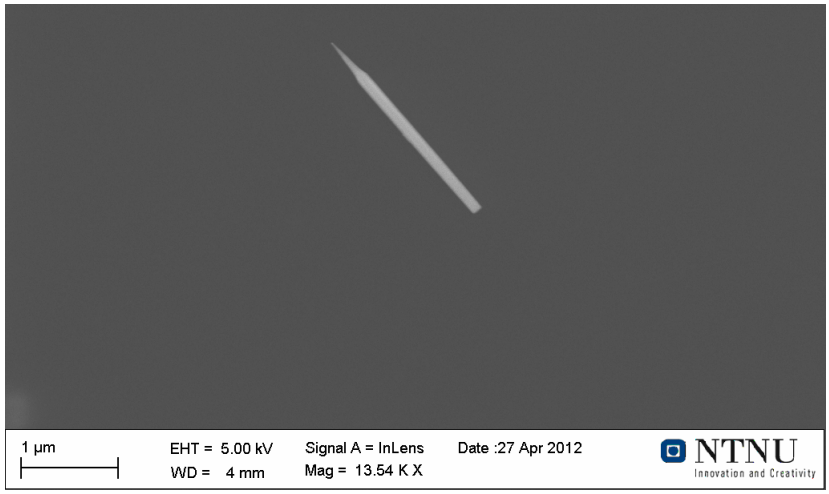


*Fig. 4.1:* SEM image of NW213. The NW has a constant diameter and a tapered tip. Dimensions: l = 2 $\mu$m, d = 120 nm.

together with the original Varshni model.

For NW213 and NW221, the peaks of the low-energy Lorentzian were traced as a function of temperature and curve fitted to the modified Varshni model, see Fig. 4.4. This gave a peak energy of 1.521 eV when extrapolating to 0K. In NW311, the temperature dependence of the low-energy peak was found only below 100 K, above which the peak was no longer resolved. These data are shown in the discussion section (Fig. 5.3). Curve fitting of these data gave a peak energy of 1.519 eV at 0K. NW311 was also the only NW to give measurable PL at room temperature.

To compare the three wires measured, the main peak energies are plotted together in Fig. 4.5. NW213 and NW221 show similar energies at 0 K, but have different slopes at higher temperatures. NW311 starts around 7 meV higher, but shows a similar slope to NW221.

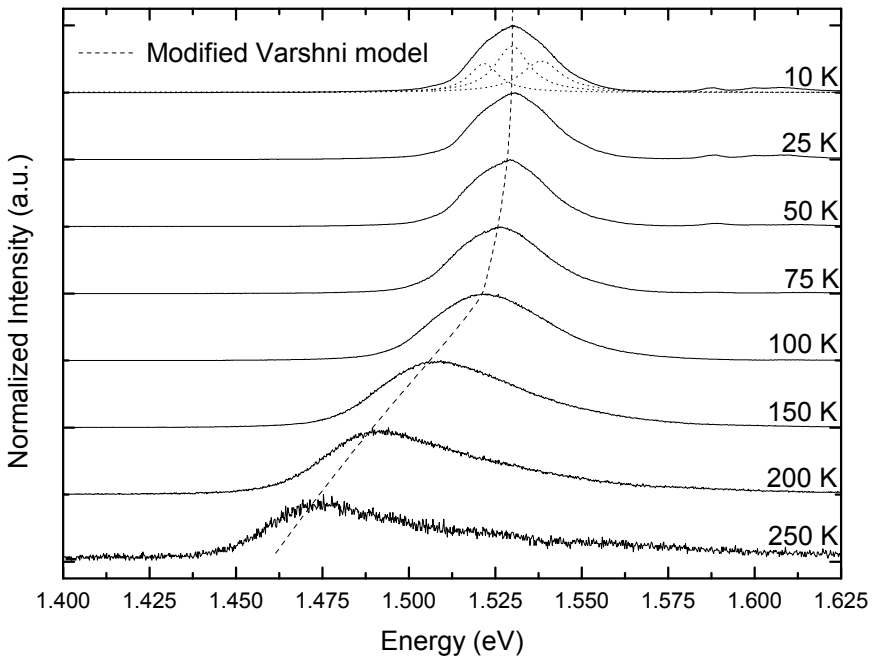


*Fig. 4.2:* Normalized temperature dependence NW213. The modified Varshni equation is fitted to the peak intensities, which is shown in detail in Fig. 4.3.

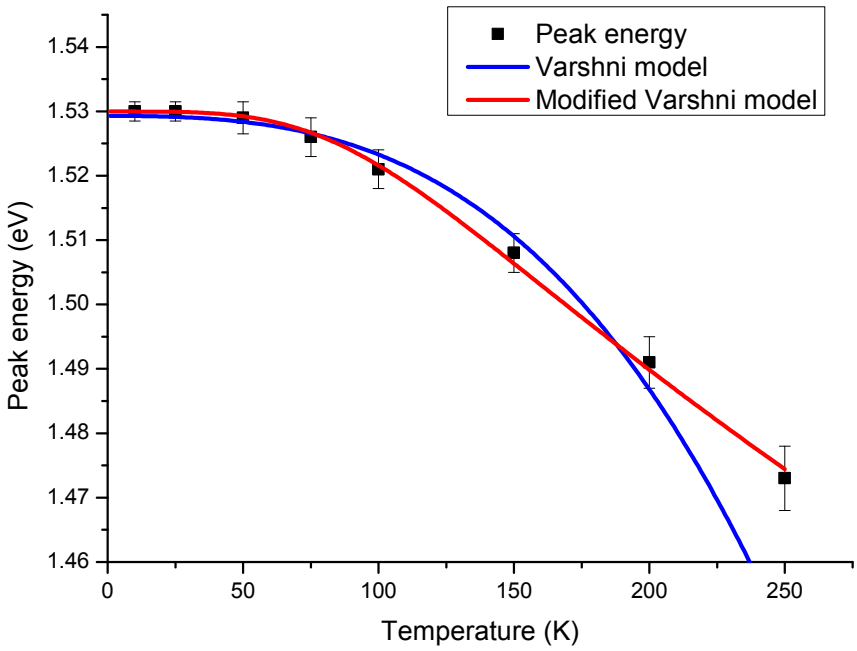


*Fig. 4.3:* Temperature dependence of peak intensities in NW213, with the fitted curves of the Varshni model (blue) and the modified Varshni model (red). The fit parameters are given in Tab. 4.1.

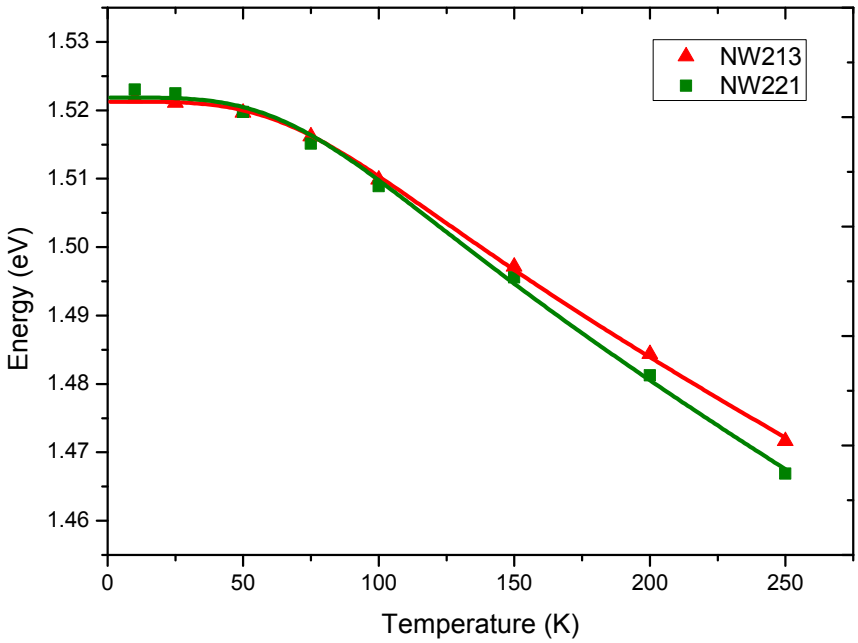


*Fig. 4.4:* Modified Varshni model, comparing the low energy peaks in NW213 and NW221.

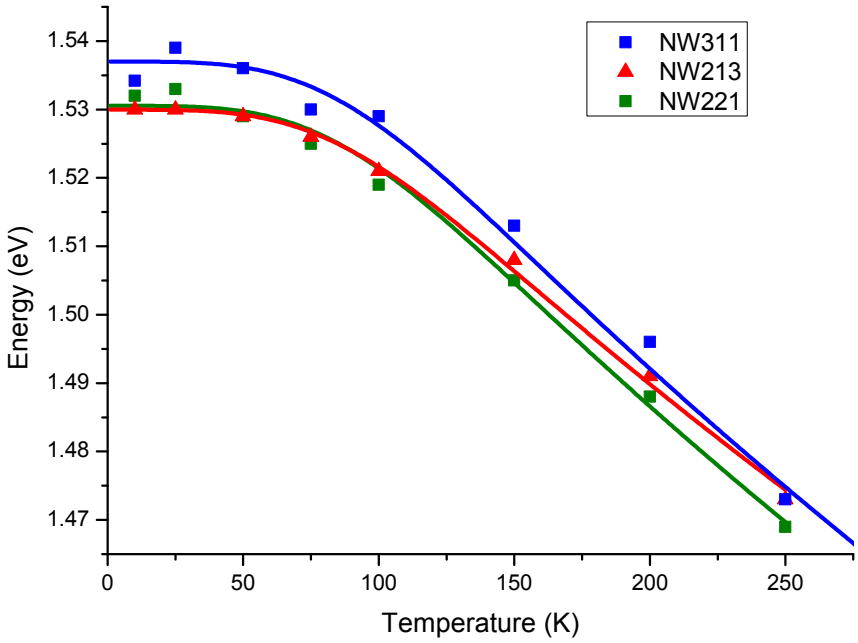


*Fig. 4.5:* Modified Varshni model, comparing the main peak NW311, NW213 and NW221. While NW213 and NW221 show similar energies at low energies, they show different slopes at higher temperatures. NW311 is nearly parallel to NW221, but at a higher energy. The fit parameters can be found in Tab. 4.1.

*Tab. 4.1:* Fit parameters for the modified Varshni model.

| NW | $E_0$ (eV) | $\alpha$ (eV/K) | $\beta$ ($K^3$) |
|---|---|---|---|
| 213 | 1.5305 | 2.75e-4 | 2e+6 |
| 221 | 1.5294 | 2.51e-4 | 2e+6 |
| 311 | 1.537 | 2.8e-4 | 2e+6 |

## *4.2 Intensity*

Normalized spectra from NW213 is presented in a stacked diagram with increasing excitation intensity (Fig. 4.6). The temperature was kept below 10 K. Excitation intensities from 570 W/cm$^2$ to 57 kW/cm$^2$ was used. The spectra were measured without polarization control and especially at higher powers, weaker shoulder peaks may hence not be clearly visible.

The peak positions used in the Varshni plots are marked with dashed lines. As one can see, the peaks are present at all intensities, whereas a third peak appears at around 28 kW/cm$^2$. Small peaks can also be seen at around 1.595 eV, which are assigned to AlGaAs emissions. The intensity from these peaks remains fairly constant with increasing excitation intensity. As can be seen in Fig. 4.2, the peaks are quenched at higher temperatures.

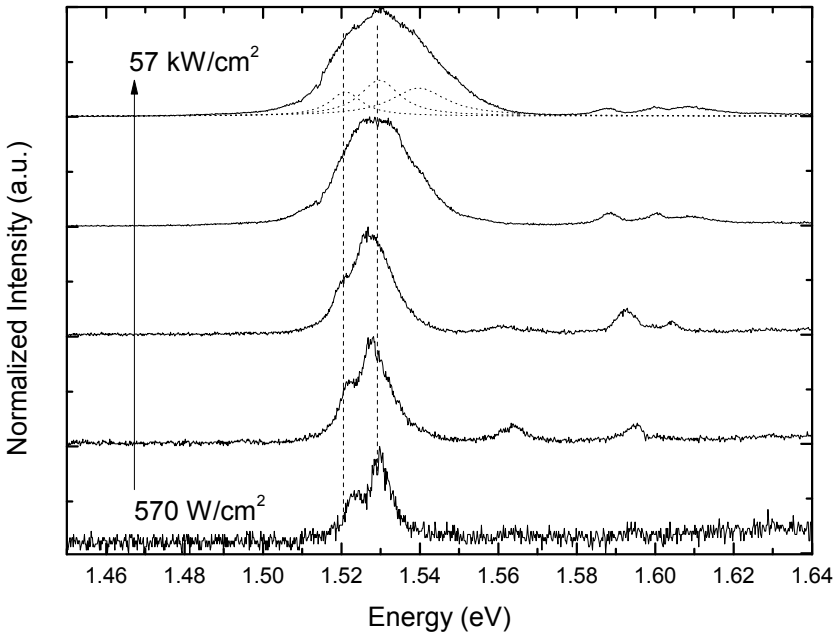


*Fig. 4.6:* Stacked PL spectra of NW213 with excitation intensities from 570 W/cm$^2$ to 57 kW/cm$^2$. The dashed lines identify the peaks fitted with the modified Varshni equation. A third peak appears at 1.54 eV for higher intensities. AlGaAs emissions with increasing energies (1.59-1.61 eV) appear when the intensity is increased, which are independent of the excitation intensity.

## *4.3 Polarization*

The polarization measurement were executed as described in Sec 3.2. An angular error of $\pm 5^\circ$ must be taken into account. An angular overlap of $20^\circ$ is intended to to ensure no changes in alignment have occurred in the course of the measurement. The polarization measurements are all done under similar conditions with excitation intensities below 50 kW/cm$^2$.

The false color plots are put together of 21 spectra (center wavelength 820 nm), taken at different compensator angles. The angles in the plots are calibrated for NW orientation. The PL intensity is hence plotted as a function of energy and polarization orientation with respect to the NW axis, where the color scale ranges from blue to red with increasing intensity. Each spectrum is also curve fitted with a set of Lorentzians, which are numerically integrated. The integrated intensity of each peak is then least-square fitted with Eq. 3.17, as explained in Sec. 3.2.2. The resulting plots show the integrated intensities of one Lorentzian, as it appears at an angle to the NW axis, together with the fit of the $\sin^2$-function. The fit parameters determine the angle of polarization, with respect to the NW axis.

The differences and similarities between the three NWs measured, will be presented in the following section. False color plots will be presented to get an overview of the main peaks. The $\sin^2$-plots are then meant to quantize the polarization of each peak.

### *4.3.1 Polarization at 10 and 50 K.*

False color plots of NW221 and NW213 are shown in Fig. 4.7 and 4.8. The main peak is polarized parallel to the NW axis in NW213, whereas it appears at $20^\circ$ in NW221. Both NWs exhibit a perpendicular peak at $\sim$1.515 eV at 10 K. At 50 K, an additional perpendicular peak, at $\sim$1.54 eV, appears in both plots, as well.

In general, the NW311 false color plot shows wider lines than the two wires shown above. Also, all peaks seem to be polarized similarly at $60^\circ$ to the NW. A more pronounced AlGaAs polarization (at $\sim$1.61 eV) can also be observed at 10 K, being polarized similar to the GaAs-related peaks.

The results from the curve fitting of NW213 are shown in Fig. 4.10. The fitting parameters for all three wires i.e. the peak energies and their polarization, are presented in Table 4.2 (10 K)and Table 4.3 (50 K). The $\sin^2$-plots show what was indicated in Fig. 4.8: The main peak is fitted with two Lorentzians and is close to parallel to the NW. The low-energy peak is polarized at $81.6^\circ$, which within the experimental error is close to

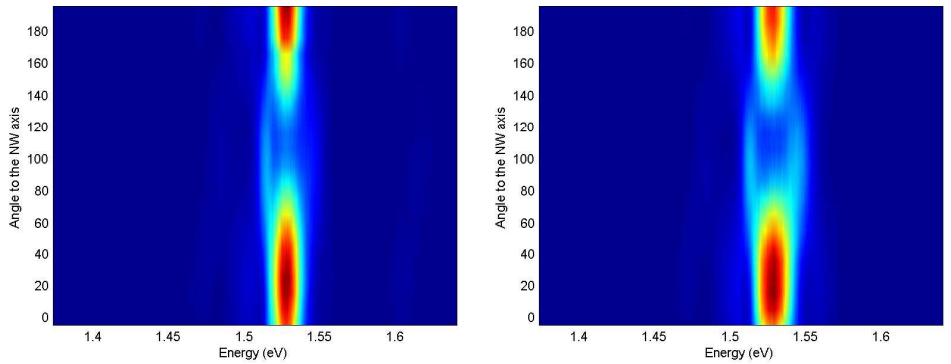


*(a)* NW221 10K *(b)* NW221 50K

*Fig. 4.7:* False color plot of NW221 at 10 K and 50 K. The main peak at ∼1.53 eV exhibits a maximum at around 20°, at both temperatures. A weaker line, which appears at both temperatures, (∼1.515 eV) is polarized almost perpendicular to the NW. In the 50 K plot, a second perpendicular peak is observed closer to 1.55 eV. Spectral broadening is also observed at 50 K.

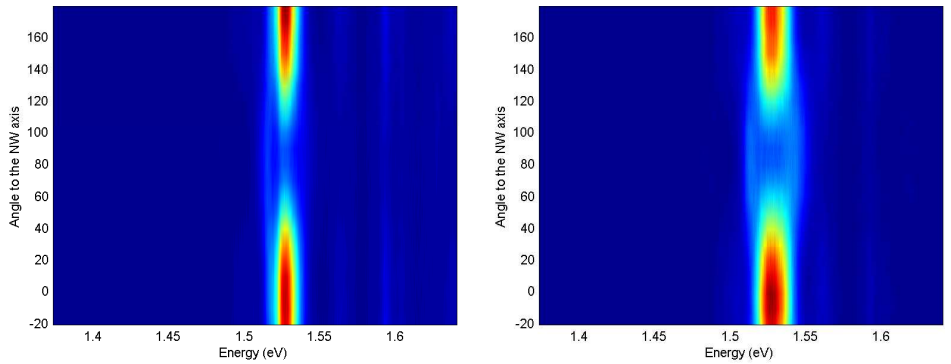


*(a)* NW213 10K *(b)* NW213 50K

*Fig. 4.8:* False color plot of NW213 at 10 K and 50 K. The main peak at ∼1.53 eV exhibits a maximum almost parallel to the NW, at both temperatures. A weaker line, which appears at both temperatures, (∼1.515 eV) is polarized almost perpendicular to the NW. In the 50 K plot, a second perpendicular peak is observed closer to 1.55 eV. Spectral broadening is also observed at 50 K.

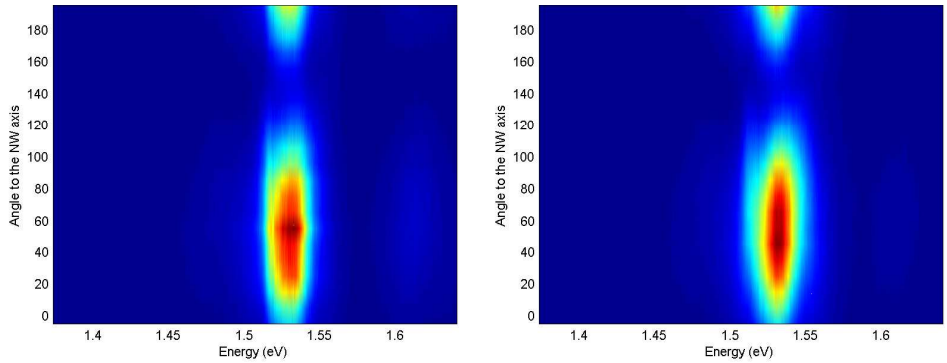


*(a)* NW311 10K

*(b)* NW311 50K

*Fig. 4.9:* False color plot of NW311 at 10 K and 50 K. The main peak at ∼1.53 eV exhibits a maximum at around 20°, at both temperatures. A weaker line, which appears at both temperatures, (∼1.515 eV) is polarized almost perpendicular to the NW. In the 50 K plot, a second perpendicular peak is observed closer to 1.55 eV. Spectral broadening is also observed at 50 K.

perpendicular. From Table 4.2, one can see that NW221 shows similar behavior, but that the main peak is polarized slightly off the parallel axis. The curvefitting method has difficulties resolving closely spaced peaks, and the average angle of the 1.527 eV and 1.532 eV peaks, is hence more valuable. Note that the total peak (Fig. 4.10a) is the sum of all contributions, regardless of their polarization direction.

At 50 K, a four-Lorentzian fit was used to investigate the 1.54 eV peak, seen in the false color plots of NW221 and NW213. The results are given in Table 4.3, which shows that the peak is polarized parallel to the 1.519 eV peak i.e. perpendicular to the NW. The $\sin^2$-plots from NW213 are presented in Fig. 4.11. The perpendicular nature of the side peaks to the main peak can clearly be observed.

As NW311 did not show any prominent side peaks, three Lorenzians was sufficient to get a good fit also at 50 K. The polarization of ∼60° is more consistent at 50 K, where the 1.519 eV-peak polarization is parallel to the higher energy peaks.

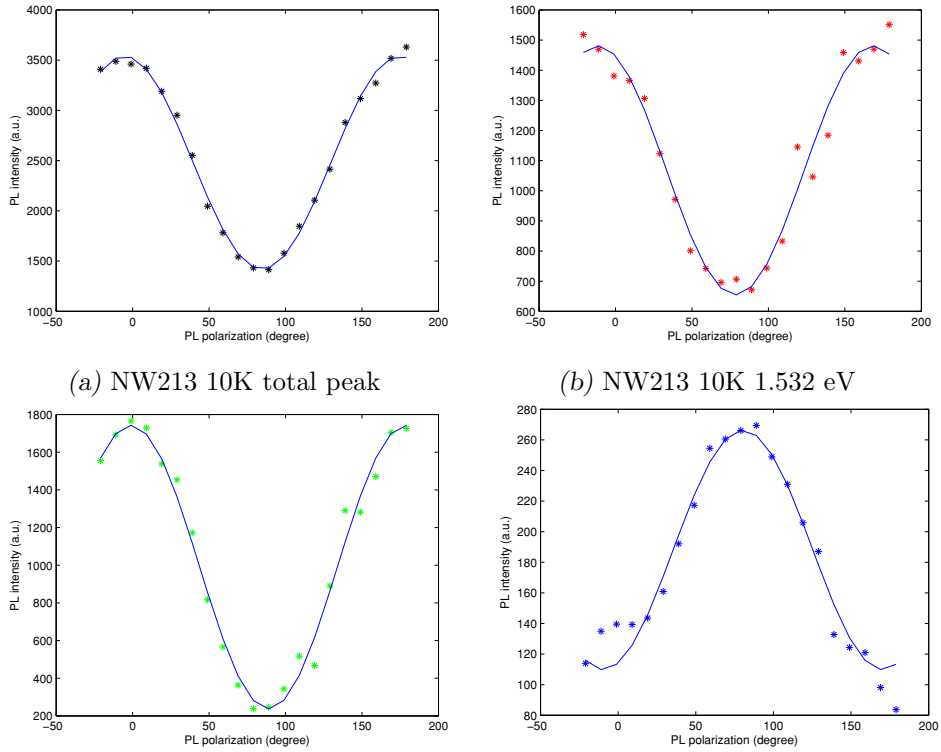


*(a)* NW213 10K total peak

*(b)* NW213 10K 1.532 eV

*(c)* NW213 10K 1.527 eV

*(d)* NW213 10K 1.519 eV

*Fig. 4.10:* NW213 $\sin^2$-fits of the integrated intensities of each Lorentzian, at 10 K. Coloured dots are the data and the blue lines are the fitted curves. The plots show that the two high-energy peaks are polarized parallel to the NW, while the 1.519 eV peak is polarized perpendicular.

*Tab. 4.2:* Polarization data at 10 K.

| NW221 | Peak energy (eV) | Angle to NW (degree) |
|---|---|---|
| | 1.519 | 90.1 |
| | 1.527 | 14.7 |
| | 1.532 | 36.7 |
| | total | 28.7 |
| NW213 | Peak energy (eV) | Angle to NW (degree) |
| | 1.519.1 | 81.6 |
| | 1.527 | 10.4 |
| | 1.532 | 2.4 |
| | total | 5.4 |
| NW311 | Peak energy (eV) | Angle to NW (degree) |
| | 1.519 | 68.8 |
| | 1.527 | 63.5 |
| | 1.532 | 43.6 |
| | total | 59.2 |

*Tab. 4.3:* Polarization data at 50 K.

| NW221 | Peak energy (eV) | Angle to NW (degrees) |
|---|---|---|
| | 1.519 | 87.7 |
| | 1.527 | 23.5 |
| | 1.532 | 23.8 |
| | 1.54 | 87.9 |
| | total | 34.8 |
| NW213 | Peak energy (eV) | Angle to NW (degrees) |
| | 1.519 | 83.5 |
| | 1.527 | 1 |
| | 1.532 | 1.9 |
| | 1.54 | 89.3 |
| | total | 2 |
| NW311 | Peak energy (eV) | Angle to NW (degrees) |
| | 1.519 | 65.5 |
| | 1.525 | 65 |
| | 1.532 | 57.7 |
| | total | 61.6 |

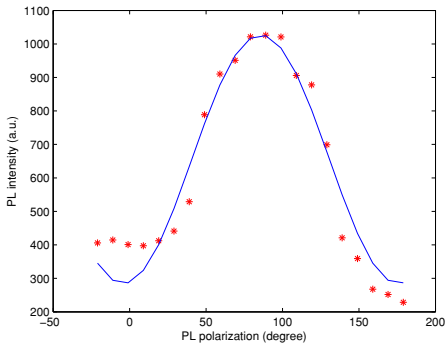


*(a)* NW213 50K 1.54 eV

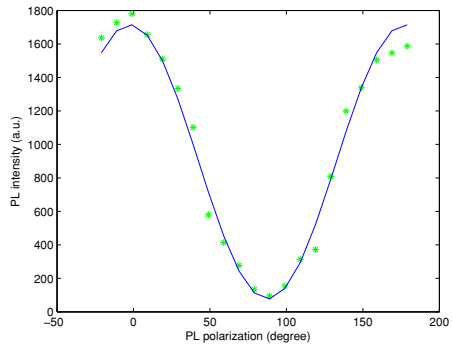


*(b)* NW213 50K 1.53 eV

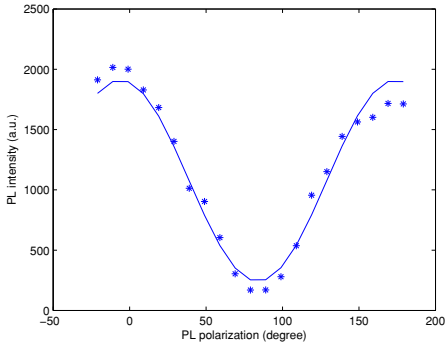


*(c)* NW213 50K 1.53 eV

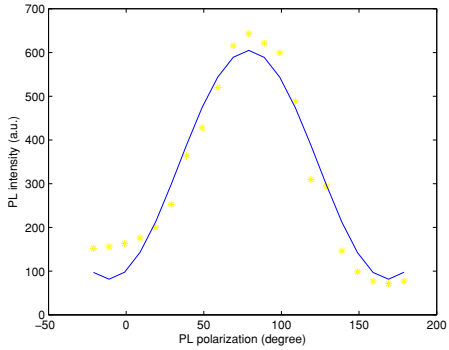


*(d)* NW213 50K 1.51 eV

*Fig. 4.11:* NW213 $\sin^2$-fits of the integrated intensities of each Lorentzian, at 50 K. Coloured dots are the data and the blue lines are the fitted curves. The plots show that the two high-energy peaks are polarized parallel to the NW, while the 1.51 eV and 1.54 eV peaks are polarized perpendicular.

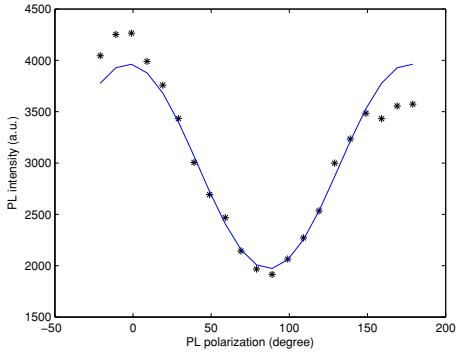


*Fig. 4.12:* NW213 50K total peak

### 4.3.2 *Intensity dependent polarization*

To gain a better insight in the effect of band filling in the GaAs insert, a second set of polarization measurements were conducted. The three NWs were excited with intensities in the range 2.9-570 kW/cm$^2$ to investigate the effect in both directions. The false color plots of NW213 and NW221 can be seen in Fig. 4.13 and 4.14, respectively.

The effect of increasing the excitation intensity can be seen to cause new peaks to appear. The effect is most prominent in NW221, where new peaks appear also at lower energies (Fig. 4.14). The new peaks are polarized alternately parallel and perpendicular. The peak appearing at 20° in NW221 previously, is now more parallel. Whereas the 1.53 eV peak remains the strongest at all intensities in NW213, the 1.55 eV peak becomes stronger in NW221. The effect of alternating in polarization was not observed NW311 (not shown). There, new peaks appear, but they are all polarized similarly.

## 4.4 *Time-resolved photoluminescence*

The measured lifetimes in NW311 are shown in Table 4.4. At some temperatures/excitation levels, the lifetimes in NW221 were difficult to find from the measured data because of poor intensity. However, the lifetimes found were consistent with the results in NW311. Lifetimes were not measured in NW213. The NWs were excited with intensities of 5.7 kW/cm$^2$ and 23 kW/cm$^2$.

The two peaks at 1.519 eV and 1.53 eV were identified in the streak camera image, and curve fitted with a double exponential. When only a short interval around the peak energy was chosen, only a single exponential contributed in the fitted curve. The resulting lifetimes, at increasing temperatures, are monotonically decreasing.

At temperature above 50 K, the lifetimes measured at the lower intensity showed an increasing signal right after excitation. This can be seen in Fig. 4.15, where also the effect of low signal intensity is evident. Below 50 K, the measured lifetimes were found to be longer than at higher intensities. At 200 K, a slight increase is first observed, before the signal decays.

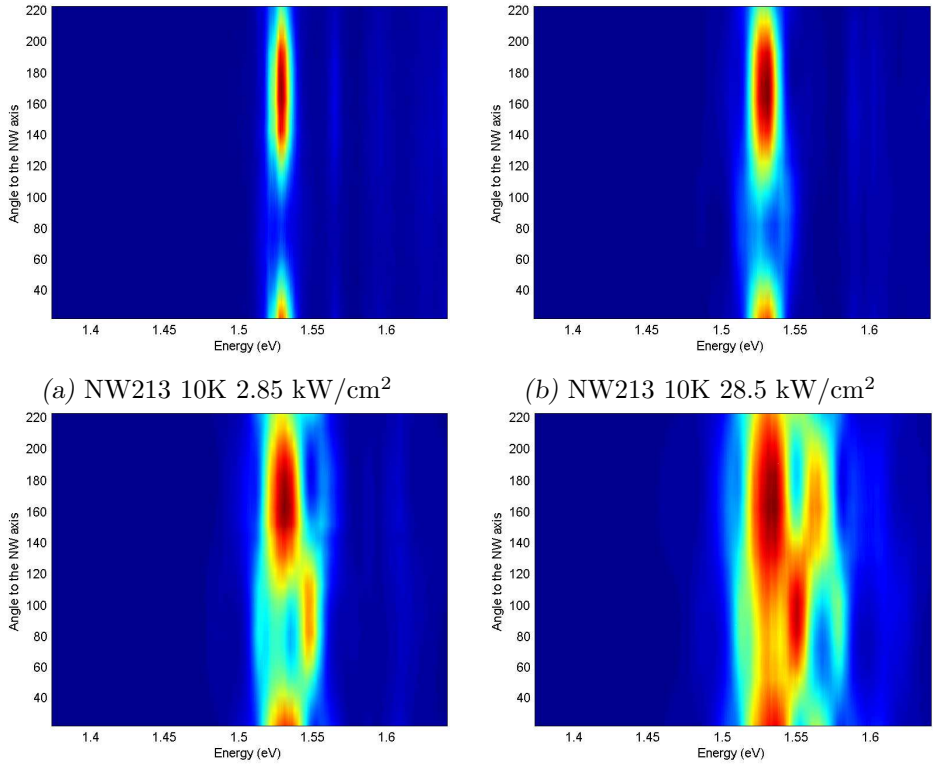


*(a)* NW213 10K 2.85 kW/cm$^2$

*(b)* NW213 10K 28.5 kW/cm$^2$

*(c)* NW213 10K 114 kW/cm$^2$

*(d)* NW213 10K 570 kW/cm$^2$

*Fig. 4.13:* NW213 false-color plots at different excitation intensities. New peaks appear with alternating polarization (parallel and perpendicular.

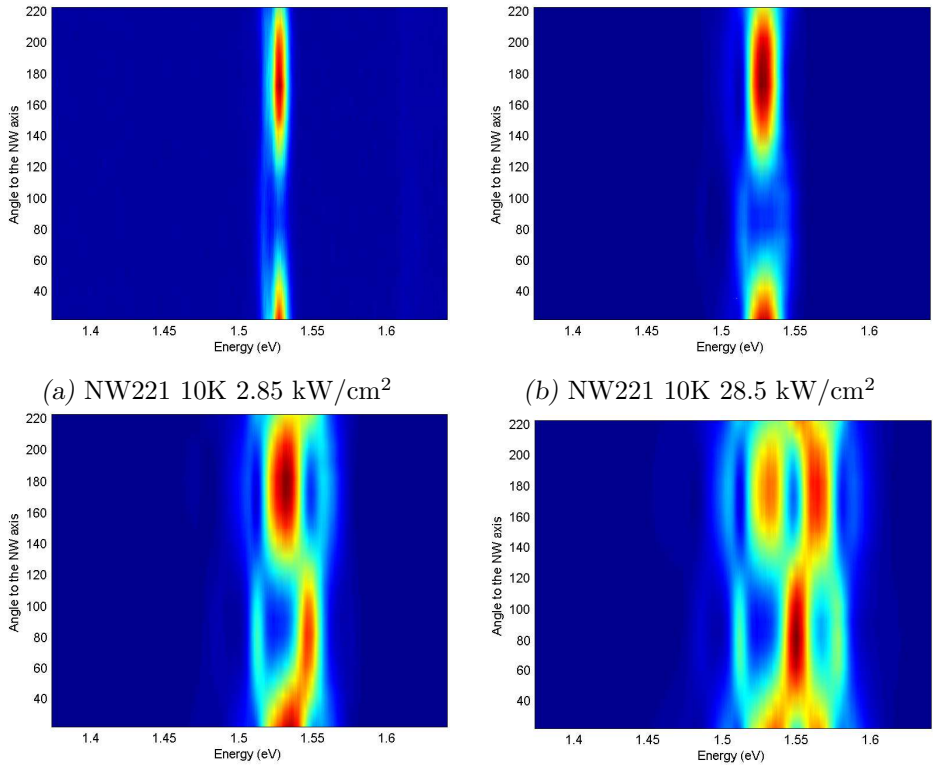


*(a)* NW221 10K 2.85 kW/cm$^2$

*(b)* NW221 10K 28.5 kW/cm$^2$

*(c)* NW221 10K 114 kW/cm$^2$

*(d)* NW221 10K 570 kW/cm$^2$

*Fig. 4.14:* NW221 false-color plots at different excitation intensities. New peaks appear with alternating polarization (parallel and perpendicular), at both higher and lower energies.

*Tab. 4.4:* The measured lifetimes at two peak energies, as a function of temperature. The 1.53 eV peak has longer lifetimes in general. Both are decreasing monotonically with increasing temperature. The excitation intensity was 23 kW/cm$^2$.

| **Temperature (K)** - Peak energy | **Lifetime (ns)** 1.519 eV | **Lifetime (ns)** 1.53 eV |
|---|---|---|
| 10 | 2.89 | 11.63 |
| 25 | 2.12 | 6.41 |
| 50 | 1.23 | 4.64 |
| 100 | 1.09 | 2.03 |
| 150 | 0.72 | 0.72 |
| 200 | 0.17 | 0.297 |

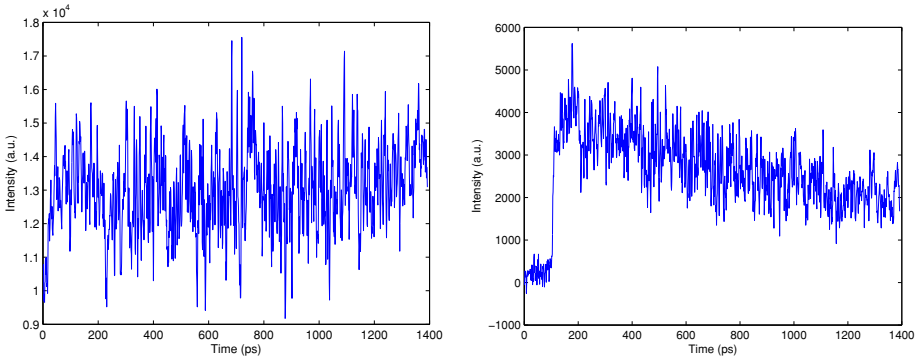


*(a)* 100 K *(b)* 200 K

*Fig. 4.15:* Measured transient in NW311 at 100 K and 200 K, with an excitation intensity of 5.7 kW/cm$^2$. The signal increases after excitation.

# 5. DISCUSSION

Temperature, intensity and polarization dependent PL measurements have been conducted on AlGaAs NWs with axial GaAs inserts. Based on the results presented in Sec. 4, two possible models are presented (Sec. 5.2 and 5.3) and discussed subsequently . First, the results are discussed from a general point of view. Comparisons of the three NWs and experimental details are included in this section.

## *5.1 General discussion of the results*

Because of the similar properties of AlGaAs and GaAs, HRTEM is unable to resolve the two materials. The discussion is therefore based solely on PL measurements. Further, the temperature and intensity measurements were done without polarization control. The relative intensity of differently polarized emissions, may therefore be an obstacle for resolving the different peak components from each other. The temperature dependence was fitted with both the original Varshni model (Eq. 3.23) and the modified one (Eq. 3.24), see Fig. 4.3. The superior fit of the modified Varshni model, motivates the use of this equation when comparing the temperature dependencies.

In the SEM images captured of the three NWs, it was found that they all have the same geometry, and should thus be expected to exhibit similar properties. Nevertheless, there are some discrepancies to be discussed. As was seen in Fig. 4.5, the temperature dependent behaviour of the three wires is not identical. Where NW311 and NW221 give high temperature slopes similar to available WZ data [15], NW213 shows a flatter slope. The slope in zincblende GaAs has however been shown to be steeper [36]. From Sec. 3.3, the behaviour in NW213 should be caused by a changed electron lattice interaction. This explanation is further corroborated by the low-energy peaks in Fig. 4.4 which exhibit the same slope as the corresponding main peak.

The temperature dependence was investigated further by curve fitting

the spectra with three Lorentzians. The peak energies of the Lorentzians were plotted together with bulk WZ GaAs data from [15]. The results for NW213 and NW311 when exciting with 57 kW/cm$^2$ can be seen in see Fig. 5.1 and 5.2, respectively. The low energy peaks generally lie above the reference data at low temperature and approach these at 100 K. This may be attributed to high excitation effects, where a blue shift of the exciton can be expected. The high energy peaks increase in energy at 200 K, which is believed to be a new emission. From the similar behaviour of the three peaks, it can be argued that they come from similar behaving emitters. For NW311 the temperature dependence with a lower excitation density (5.7 kW/cm$^2$) was investigated, as well (Fig 5.3). Because the high energy peak was not resolved at this intensity, only two Lorentzian was used in the curve fitting. Only the low energy peaks are shown, which shows an excellent fit to the reference data. This enforces the assumption that the free exciton is blue shifted by high excitation effects, which simultaneously cause higher energy peaks to appear. Although, the low energy peak was not resolvable above 100 K, where the main peak dominated the spectra, it is believed to be the free exciton in WZ GaAs. This is confirmed by the perpendicular polarization of this peak (see selection rules in Sec. 2.6). The polarization measurements on NW213 and NW221 are in agreement with this model, with perpendicular peaks at this energy. In NW311, however, the 1.519 eV peak is polarized at 60° to the NW axis. Other effects are needed to explain this, such as the dielectric mismatch effect or a high concentration of stacking faults, which make the emission more parallel. In all three wires the possibility of other contributions to this peak can not be excluded.

The 1.519 eV and 1.53 eV peaks are present at all temperatures and intensities, where the latter is polarized differently in all three wires. The polarization of this peak would hence need to be dependent on special conditions in each case. Quantum wells at the AlGaAs-GaAs interface is a plausible explanation here. The 1.54 eV peak, appearing only in NW213 and NW221, is perpendicular, as well. This indicates that the same selection rules apply for this transition as for the low-energy peak.

The intensity dependence in Fig. 4.6 shows that at low intensities only the two low-energy levels are emitting. The low-energy peak is attributed to the free exciton in GaAs, whereas the second may come from a quantum confinement emitter. The third peak appears first at higher intensities, indicating band filling in the first two transitions. The same can be seen for the AlGaAs peak at energies above 1.59 eV. At low intensities only the first peak is resolved, whereas a second and third peak appear as the

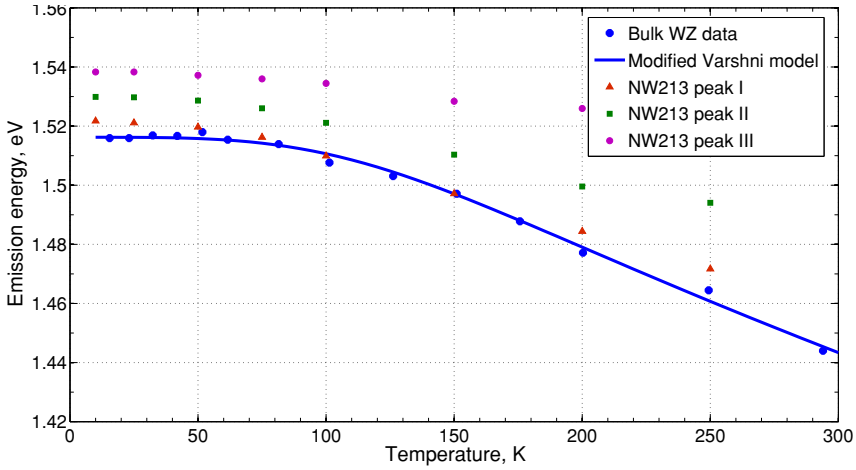


*Fig. 5.1:* Comparison of the three peaks in NW213 with data on bulk WZ GaAs [15]. The line is the fitted modified Varshni model.

intensity is increased. As the insert is filled up with carriers, the higher energy levels, believed to come from a quantum emitter, get populated and new PL peaks appear.

In the initial polarization measurements, the main peak in NW221 was polarized at 20° to the NW axis. However, in the second measurement, when doing intensity dependent polarization measurements, the same peak was found to be parallel. This may be caused by the time-resolved measurements, where high intensity infrared excitation was used. This was found to burn away other NWs and can hence be expected to have changed the structure in NW221.

The measured lifetimes up to order of magnitude longer than expected in GaAs NWs [37]. This is however, the 1.53 eV peak which is believed not to be the band-band transition. The 1.519 eV peak (2.89 ns) is well within the expected range. The reduced lifetimes at higher temperatures is expected from increased non-radiative recombination. Interestingly, the signal seems to increase with time at low intensities at 50 K and above. The effect is not consistent in all measurements and may therefore be an artefact. It has, however, been described earlier in InP NWs [38]. It is described as an effect caused by completely ionized excitons at high carrier densities. Once the average carrier density becomes lower than the Mott density, excitons reappear. Considering the GaAs inserts, the effect may originate from electrons excited in the AlGaAs filling the lower gap material.

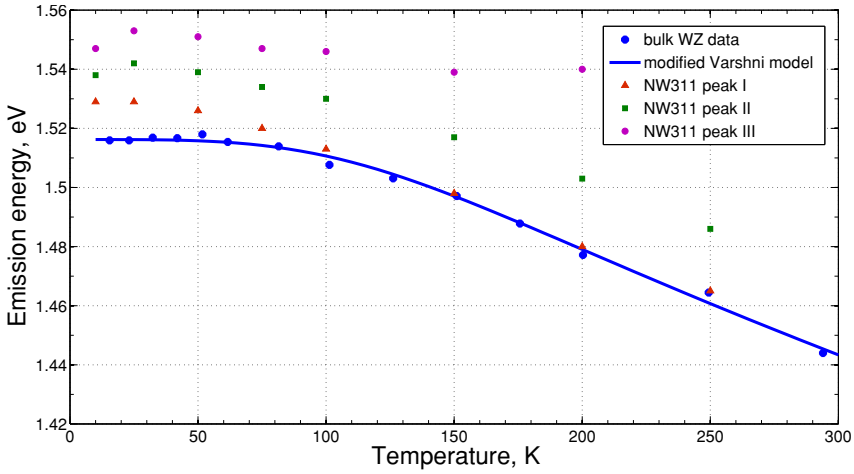


*Fig. 5.2:* Comparison of the three peaks in NW311 with data on bulk WZ GaAs [15]. The line is the fitted modified Varshni model.

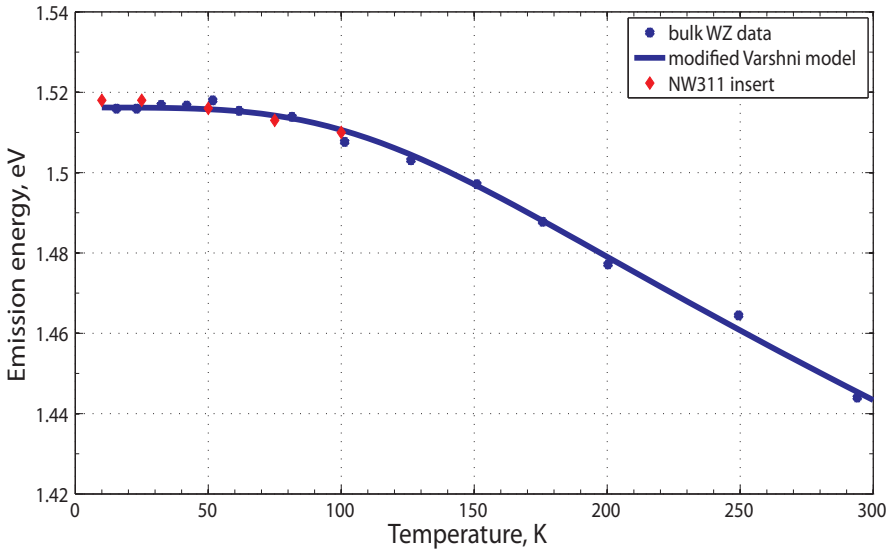


*Fig. 5.3:* Comparison of 1.519 eV peak in NW311 (low intensity) with data on bulk WZ GaAs [15]. The line is the fitted modified Varshni model.

Carriers close to the insert, in the space-charge region, would be pulled into the GaAs and increase the concentration.

## *5.2 Scenario I: NW broken at insert with quantum confined GaAs in the tip*

Inspection of as-grown samples reveals a high density of NWs. This may cause the wires not to break off at the bottom, but rather at a higher point. The proposed explanation of the results in this section assumes that the NWs have an un-passivated GaAs surface at the bottom, where the wire broke off. An illustration of the result is shown in Fig. 5.4.

The expected free exciton emission is 1.515 eV, which is polarized perpendicular to the wire. The 1.519 eV peak appearing in the measurements, which also is perpendicular, indicates that the insert is present. Band filling caused by the high excitation intensity may be be the explanation for the small blue shift. This effect can be seen as to compete with non-radiative recombination at surface states on the open GaAs surface, which explains the weak signal. This is supported by the fact that this emission is quenched above 100 K, see Fig. 5.3.

To explain the stronger 1.53 eV peak, the growth procedure is reviewed. After growing the AlGaAs NW with a GaAs insert, the AlGaAs was passivated again with a thin layer of GaAs growing radially along the wire. However, with the gold catalyst particle still at the tip, the procedure will simultaneously grow a short GaAs segment at the tip. The size of this segment could cause quantum confinement of charge carriers, which in turn can explain the higher energy emission (Fig. 2.2 and Sec. 2.4.3). Quantum confinement could also explain the different polarizations of this peak, since the effect changes the band structure and selection rules.

Earlier results have, however, shown that NWs grown under the same conditions, but without an insert, show no PL signal at all. On the contrary, the wires without a tip showed no PL signal in this study. Also, the measured NWs have differently shaped tips, which could explain the different 1.53 eV polarizations. However, this factor influences the effective bandgap, as well, making it difficult to explain the same peak appearing in all wires.


*Fig. 5.4:* NW broken at the insert, with quantum confined GaAs at the tip.

## *5.3 Scenario II: Quantum wells in the gradual AlGaAs-GaAs interface*

The second model is based on a gradual GaAs-AlGaAs transition, which is expected when switching the material composition during growth. The compositional variations at the interface can be expected to create quantum wells where charge carriers may get trapped, called the reservoir effect [39]. This is believed to arise from the different solubilities of the cations and anions in the catalyst particle, which may cause concentration oscillations from the rapid formation of a monolayer. The fluctuations have been found to appear mainly when growing AlGaAs on GaAs [40], and would hence only appear on one side. A schematic of the resulting band structure can be seen in Fig. 5.5.

Because of the small size of the GaAs insert, the amount of electrons diffusing into it from the AlGaAs are expected to be significant. This process is enhanced by increasing the excitation. As the carrier concentration in the insert increases, high excitation effects appear and the excited carriers diffusing into the insert get trapped in the quantum wells. It appears that even at the lowest intensities used in the measurements (570 W/cm$^2$), carriers are trapped in the lowest energy quantum well, corresponding to the 1.53 eV peak.

To investigate this effect further, new polarization dependent measurements were done at higher intensities up to 570 kW/cm$^2$. As can be seen in Fig. 4.13 and 4.14, even higher energy peaks were found. This indicates further filling of the insert and quantum wells, where hence new quantum wells at the interface are filled. Interestingly, the peaks are polarized alternating

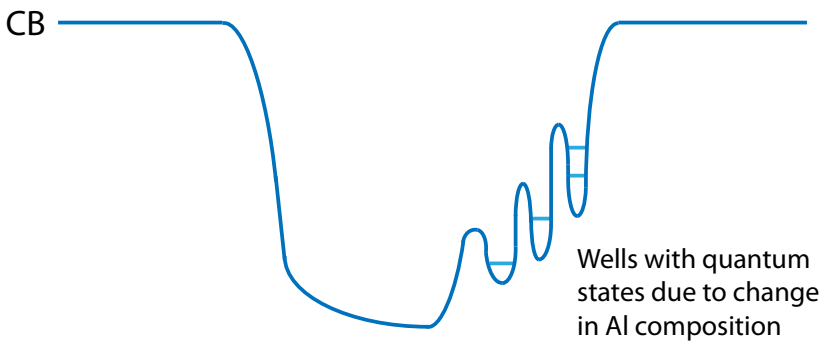


*Fig. 5.5:* Possible band structure along the insert axis, due to variations in Al composition at the insert facets.

parallel and perpendicular to the NW. It follows that different selection rules apply to the two sets of transitions. One could argue that the parallel peaks are emissions from quantum wells, while the perpendicular peaks come from features in the insert. The peak energies and their polarizations are given in Table 5.1, for NW213 and NW221. It is also worth noting that all peaks were polarized in the same direction in NW311, which could indicate a high concentration of stacking faults, as explained in Sec. 2.2.1.

To investigate the series of perpendicular peaks, the band structure around the Γ-point in WZ GaAs is shown in Fig. 5.6. From the selection rules in Fig. 2.6, the $\Gamma_{7C}$-$\Gamma_{9V}$ transition would be perpendicular. De and Pryor [6] estimate the $\Gamma_{7C}$ at 85 meV above the $\Gamma_{8C}$-band, which does not match the difference between the first two perpendicular peaks found here. However, the lattice parameter used in the calculation is incorrect, as they used the ZB value. As this would significantly affect both the position and curvature of the bands, conclusions can not be made based on these data. It is therefore possible that the perpendicularly polarized peaks represent the allowed transitions in Fig. 2.6. Ketterer et al. [10] estimates the *lh*-VB 0.103 meV below the *hh*-VB, but also claim that the lowest CB is the $\Gamma_7$-band. As reliable data is difficult to find, the proposed explanation using the selection rules can not be ruled out.

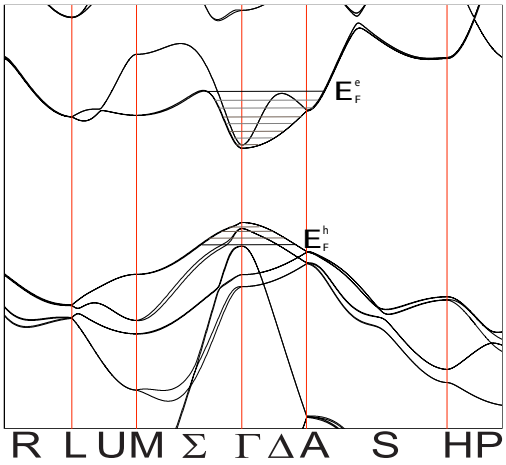


*Fig. 5.6:* Possible situation of band filling. The illustration derived from the complete band structure in Fig. 2.1. By high carrier concentration the CB can be filled to a point where other high symmetry points (L and A) are populated.

*Tab. 5.1:* Peak energies in the polarization measurements at high intensity.

| **Peak energy (eV)** (parallel) | **Energy shift (meV)** (relative to energy above) |
|---|---|
| 1.466 | |
| 1.504 | 38 |
| 1.533 | 29 |
| 1.564 | 31 |
| 1.589 | 25 |
| **Peak energy (eV)** (perpendicular) | **Energy shift (meV)** (relative to energy above) |
| 1.486 | |
| 1.512 | 26 |
| 1.55 | 38 |
| 1.578 | 28 |

## 5.4 Conclusion and Outlook

AlGaAs/GaAs NW heterostructures hold much promise in the development of NW devices. Such NW heterostructures are important, as they comprise the NW equivalent to GaAs/AlGaAs thin films, which have widespread use in device technology. It is therefore in paramount to study the highly controversial properties of WZ GaAs in order to facilitate the development of this technology. The AlGaAs NWs with axial GaAs inserts are hence an interesting system to investigate to gain a better insight in the fundamental properties of these materials.

Through polarization, temperature and intensity dependent $\mu$-PL measurements the NWs were characterized and the results interpreted. The WZ GaAs emission from the insert was identified, but the spectra were dominated by stronger emissions with higher energies. Arguments were found that explains these peaks from Al composition oscillations in the GaAs insert.

It is clear that the perpendicular nature of the emissions is a property of WZ crystals, since ZB emissions are polarized parallel as a result of the dielectric effect. The peaks measured, polarized parallel to the NWs, were attributed to a series of quantum wells at the interface, with different energies. The quantum confinement affects the polarization, which together with stacking faults and disorder make the dielectric effect dominate the emission.

The characterization of NWs is significantly simplified when HRTEM images are available. Without the structural information provided from these measurements, uncertainties are often left open. Different ways to achieve the needed contrast to resolve GaAs and AlGaAs include:

- A higher Al content in the NW would give better TEM contrast due to an increased scattering difference between the two materials. However, an increased Al concentration makes NW growth difficult to realize.

- An AlAs barrier around the insert could be used to mark the insert, as this material is resolvable.

- HAADF-STEM could be used to investigate the crystal structure. The technique involves extensive modeling and requires the NWs to be dispersed on a graphene covered TEM-grid. This makes PL measurement difficult because it relies on reflection from the surface to orientate on the sample.

This type of structures should be further investigated in order to elaborate on the conclusions made in this thesis.

# BIBLIOGRAPHY


[1] Peidong Yang, Ruoxue Yan, and Melissa Fardy. Semiconductor nanowire: what's next? *Nano letters*, 10(5):1529–36, May 2010.

[2] Yi Cui, Xiangfeng Duan, Jiangtao Hu, and Charles M. Lieber. Doping and Electrical Transport in Silicon Nanowires. *The Journal of Physical Chemistry B*, 104(22):5213–5216, June 2000.

[3] X Duan, Y Huang, and R Agarwal. Single-nanowire electrically driven lasers. *Nature*, 421(January):241–246, 2003.

[4] Yu Huang, Xiangfeng Duan, and Charles M Lieber. Nanowires for integrated multicolor nanophotonics. *Small (Weinheim an der Bergstrasse, Germany)*, 1(1):142–7, January 2005.

[5] Erik Garnett and Peidong Yang. Light trapping in silicon nanowire solar cells. *Nano letters*, 10(3):1082–7, March 2010.

[6] A. De and Craig E. Pryor. Predicted band structures of III-V semiconductors in the wurtzite phase. *Physical Review B*, 81(15), April 2010.

[7] D L Dheeraj, H L Zhou, A F Moses, T B Hoang, A T J Van Helvoort, B O Fimland, and H Weman. Heterostructured III-V Nanowires with Mixed Crystal Phases Grown by Au-assisted Molecular Beam Epitaxy. In Paola Prete, editor, *Nanowires*, number March, chapter 2, pages 23–50. 2010.

[8] Thang B. Hoang, a. F. Moses, H. L. Zhou, D. L. Dheeraj, B. O. Fimland, and H. Weman. Observation of free exciton photoluminescence emission from single wurtzite GaAs nanowires. *Applied Physics Letters*, 94(13):133105, 2009.

[9] D. Spirkoska, Al. Efros, WRL Lambrecht, T. Cheiwchanchamnangij, A. Fontcuberta i Morral, and G. Abstreiter. Valence band

structure of polytypic zinc-blende/wurtzite GaAs nanowires probed by polarization-dependent photoluminescence. *Physical Review B*, 85(4):1–11, January 2012.

[10] Bernt Ketterer, Martin Heiss, Emanuele Uccelli, Jordi Arbiol, and Anna Fontcuberta i Morral. Untangling the electronic band structure of wurtzite GaAs nanowires by resonant Raman spectroscopy. *ACS nano*, 5(9):7585–92, September 2011.

[11] Jing Liqiang, Qu Yichun, Wang Baiqi, Li Shudan, Jiang Baojiang, Yang Libin, Fu Wei, Fu Honggang, and Sun Jiazhong. Review of photoluminescence performance of nano-sized semiconductor materials and its relationships with photocatalytic activity. *Solar Energy Materials and Solar Cells*, 90(12):1773–1787, July 2006.

[12] AL Linsebigler, Guangquan Lu, and John T. Yates. Photocatalysis on TiO2 surfaces: principles, mechanisms, and selected results. *Chemical Reviews*, pages 735–758, 1995.

[13] Kittel. *Introduction to solid state physics*. John Wiley & Sons, Inc., 8. edition, 2005.

[14] Harald Ibach and Hans Lüth. *Festkörperphysik*. Springer, 3 edition, 2003.

[15] Lyubomir Ahtapodov, Jelena Todorovic, Phillip Olk, and Terje Sund Mjaaland. A Story Told by a Single Nanowire : Wurtzite GaAs and Optical Quality Achievable with Au- assisted MBE Growth. *(in preparation)*.

[16] M Murayama. Chemical trend of band offsets at wurtzite/zinc-blende heterocrystalline semiconductor interfaces. *Physical Review B*, 49(7), 1994.

[17] Wang Peng, F. Jabeen, B. Jusserand, J. C. Harmand, and M. Bernard. Conduction band structure in wurtzite GaAs nanowires: A resonant Raman scattering study. *Applied Physics Letters*, 100(7):073102, 2012.

[18] R Dingle, DD Sell, and SE Stokowski. Absorption, reflectance, and luminescence of GaN epitaxial layers. *Physical Review B*, 4(August), 1971.

[19] Steffen Breuer, Carsten Pfüller, Timur Flissikowski, Oliver Brandt, Holger T Grahn, Lutz Geelhaar, and Henning Riechert. Suitability of Au- and self-assisted GaAs nanowires for optoelectronic applications. *Nano letters*, 11(3):1276–9, March 2011.

[20] P Caroff, KA Dick, J Johansson, and ME Messing. Controlled polytypic and twin-plane superlattices in III-V naowires. *Nature*, 4(November 2008), 2008.

[21] TB Hoang, LV Titova, and HE Jackson. Imaging and optical properties of single core-shell GaAs-AlGaAs nanowires. *IEEE-NANO*, 00(c):1–3, 2006.

[22] I. Zardo, S. Conesa-Boj, F. Peiro, J. R. Morante, J. Arbiol, E. Uccelli, G. Abstreiter, and a. Fontcuberta i Morral. Raman spectroscopy of wurtzite and zinc-blende GaAs nanowires: Polarization dependence, selection rules, and strain effects. *Physical Review B*, 80(24):1–11, December 2009.

[23] H. Ruda and a. Shik. Polarization-sensitive optical phenomena in semiconducting and metallic nanowires. *Physical Review B*, 72(11):1–11, September 2005.

[24] L Van Hove. The occurrence of singularities in the elastic frequency distribution of a crystal. *Physical Review*, 11(1941), 1953.

[25] Gregory D Scholes. Insights into excitons confined to nanoscale systems: electron-hole interaction, binding energy, and photodissociation. *ACS nano*, 2(3):523–537, 2008.

[26] Gregory D Scholes and Garry Rumbles. Excitons in nanoscale systems. *Nature Materials*, 5(9):683–96, 2006.

[27] N S Sariciftci, L Smilowitz, a J Heeger, and F Wudl. Photoinduced electron transfer from a conducting polymer to buckminsterfullerene. *Science (New York, N.Y.)*, 258(5087):1474–6, November 1992.

[28] L. V. Titova, Thang B. Hoang, H. E. Jackson, L. M. Smith, J. M. Yarrison-Rice, Y. Kim, H. J. Joyce, H. H. Tan, and C. Jagadish. Temperature dependence of photoluminescence from single core-shell GaAs–AlGaAs nanowires. *Applied Physics Letters*, 89(17):173126, 2006.

[29] Albert Einstein. Zur Quantentheorie der Strahlung. *Physikalische Zeitschrift*, 18(1):121–128, May 1917.

[30] Thang Ba Hoang, Lyubov V Titova, Jan M Yarrison-Rice, Howard E Jackson, Alexander O Govorov, Yong Kim, Hannah J Joyce, H Hoe Tan, Chennupati Jagadish, and Leigh M Smith. Resonant excitation and imaging of nonequilibrium exciton spins in single core-shell GaAs-AlGaAs nanowires. *Nano letters*, 7(3):588–95, March 2007.

[31] P Vagner, M Mosko, and D. Munzar. Calculation of excitonic absorption spectrum of GaAs quantum wire free-standing in vacuum. *Acta Physica Polonica, Series A*, 92(5):1038, 1997.

[32] Y.P. Varshni. Temperature dependence of the energy gap in semiconductors. *Physica*, 34(1):149–154, January 1967.

[33] T. K. Tran, W. Park, W. Tong, M. M. Kyi, B. K. Wagner, and C. J. Summers. Photoluminescence properties of ZnS epilayers. *Journal of Applied Physics*, 81(6):2803, 1997.

[34] C. Steel and K. Razi Naqvi. Differential method in chemical kinetics. *The Journal of Physical Chemistry*, 95(26):10713–10718, December 1991.

[35] Physics-Spectra. Tsunami User's Manual: Mode-locked Ti:sapphire Laser, 2002.

[36] P Lautenschlager, M Garriga, and S Logothetidis. Interband critical points of GaAs and their temperature dependence. *Physical Review B*, 35(17):9174–9189, 1987.

[37] D. Spirkoska, J. Arbiol, a. Gustafsson, S. Conesa-Boj, F. Glas, I. Zardo, M. Heigoldt, M. H. Gass, a. L. Bleloch, S. Estrade, M. Kaniber, J. Rossler, F. Peiro, J. R. Morante, G. Abstreiter, L. Samuelson, and a. Fontcuberta i Morral. Structural and optical properties of high quality zinc-blende/wurtzite GaAs nanowire heterostructures. *Physical Review B*, 80(24):1–9, December 2009.

[38] Lyubov V Titova, Thang Ba Hoang, Jan M Yarrison-Rice, Howard E Jackson, Yong Kim, Hannah J Joyce, Qiang Gao, H Hoe Tan, Chennupati Jagadish, Xin Zhang, Jin Zou, and Leigh M Smith. Dynamics of strongly degenerate electron-hole plasmas and excitons in single InP nanowires. *Nano letters*, 7(11):3383–7, November 2007.

[39] Frank Glas, Jean-Christophe Harmand, and Gilles Patriarche. Nucleation Antibunching in Catalyst-Assisted Nanowire Growth. *Physical Review Letters*, 104(13):2–5, March 2010.

[40] M Tanaka. Atomistic models of interface structures of GaAs-AlxGa1-xAs (x= 0.2-1) quantum wells grown by interrupted and uninterrupted MBE. *Journal of Crystal Growth*, 81:2–7, 1987.